Department of Physics and Astronomy
University of Heidelberg

Bachelor Thesis in Physics
submitted by

Maja Lecher

born in Mödling (Austria)

2019

Exploring the applicability of electrodeposited copper for reducing the radon background in liquid xenon detectors

This Bachelor Thesis has been carried out by Maja Lecher at the
Max-Planck Institute für Kernphysik
under the supervision of
Priv. Doz. Dr. Teresa Marrodán Undagoitia

Abstract

The DARWIN experiment is a proposed dark matter search that is set to employ liquid xenon to detect scattering events originating from hypothetical dark matter particles (WIMPs). Being a rare-event search, the experiment requires an ultra-low background to reach its target sensitivity. The radioactive isotope ^{222}Rn emanating from the detector materials currently poses the most serious threat to the background level as it has the potential to mimic signals of the searched-for WIMP interactions. In this thesis, electrodeposited copper coatings are investigated for their potential application for reducing this background source. For this purpose, thoriated tungsten welding electrodes are coated using a variety of different coating parameters. It was shown that while some reduction factor > 1 was generally achieved, the reduction factors are often inconsistent and the electrodeposition process not very well understood at this stage. Additionally, it was found that the activity remaining after the coating process is likely diffusion-driven.

Abstract

Das DARWIN-Experiment ist ein geplanter Dunkle Materie-Detektor, dessen Beobachtungsprinzip auf der Streuung hypothetischen WIMP-Teilchen (Weakly Interacting Massive Particles) an gewöhnlicher Materie beruht. Aufgrund der geringen erwarteten Ereignisrate ist ein niedriger Untergrund für das Erreichen der vorgesehenen Empfindlichkeit des Detektors unabdinglich. Den aktuell schwerwiegendsten Beitrag zum Untergrund liefert das radioaktive Isotop ^{222}Rn, welches Signale ähnlich denen der erwarteten WIMP-Ereignisse verursachen kann. In dieser Bachelorarbeit wird die Eignung elektrodepnierten Kupfers untersucht im Bezug auf seine Fähigkeit, diesen Untergrund zu reduzieren. Hierfür wurden thorierte Schweißelektroden aus Wolfram unter verwendung verschiedener Parameter beschichtet. Wie sich gezeigt hat sind die hiermit erreichten Reduktionsfaktoren häufig sehr inkonsistent und wird der Prozess der Elektrodeposition offenbar noch nicht vollständig verstanden. Ebenfalls wurde gezeigt, dass die Aktivität, die nach der Beschichtung übrig bleibt, mit großer Wahrscheinlich diffusionsgetrieben ist.

Contents

Chapter 1

Introduction

Despite the existence of numerous experiments corroborating the validity of the Standard Model, plenty of evidence suggests that the model is incomplete. Among the problems still unsolved is that of the nature of dark matter (DM): a postulated form of non-luminous matter invoked to account for a variety of unexplained phenomena from astrophysical observations, ranging from galaxy formation to the structure of the cosmic microwave background. A number of potential candidates have been proposed. One of the most promising contenders is the **W**eakly **I**nteracting **M**assive **P**article (WIMP), which would, in theory, pass through earth and allow the detection of nuclear recoils using noble gas detectors. Of the several running searches taking the direct approch to detection, one is the XENON experiment currently undergoing an upgrade to its fourth iteration (XENONnT). While its background level is the lowest achieved among detectors employing liquid xenon so far [14], the project's future (DARWIN) requires an even stronger background reduction. The dominant contribution to the background rate is made by trace amounts of radioactive impurities inherently present in detector materials which permanently emanate daughters of the primordial ^{238}U decay chain. These decays can produce signals that mimic those expected for a WIMP event. In order to further lower the background level it is therefore essential that these isotopes are prevented from reaching the active detector volume.

In this thesis, we study the performance of electrodeposited copper to achieve a reduction of radon emanation. The detection principle of the XENON1T detector is briefly introduced in section 1.3, followed by a discussion of their radon background in Ch. 2. The experimental methods which will be employed in this work are described in Ch. 3. Finally, the results of this investigation are presented in Ch. 4.3.

1.1 The hunt for dark matter

The journey to our understanding of dark matter as it stands today began with the recognition that not all forms of matter must necessarily be luminous, and that ”light is no real property of mass” (Bessel, 1844) [7]. This notion, while initally referring to a general class of invisible astrophysical objects only perceptible by virtue of their gravitational influence, eventually lead to the hypothesis that the standard model is incomplete.

In 1933, the Swiss astronomer Fritz Zwicky was studying the Coma galaxy cluster when he noticed a discrepancy between the mass of visible matter and the mass calculated from the cluster's velocity distribution using the virial theorem. He realized that the amount of visible matter in the cluster was not nearly sufficient to generate a gravitational field strong enough to hold it together; in fact, there would need to be around 400 times as much. Zwicky concluded that dark matter must be present in much greater quantities than luminous matter [1]. The next hint about the existence of non-luminous matter came from Vera Rubin et al. in 1978, who observed that bodies at the edge of galaxies do not move more slowly than those in the galactic center. This is inconsistent with predictions made by Newtonian mechanics, where the rotational velocities are expected to behave according to

$$v_{rot}(r) = \sqrt{\frac{GM(r)}{r}}, \tag{1.1}$$

where G is the gravitational constant, and $M(r)$ is the total amount of mass within a radius r [6].

A number of other cosmological observations, e.g. the structure of the cosmic microwave background and gravitational lensing effects, have provided further evidence for the existence of dark matter since [6]. According to current models, the universe should consist of 4.9% baryonic matter, 68.3% dark energy, and 26% dark matter [2].

1.2 Particle candidates, detection methods and current searches

Many different theories exist about the nature of dark matter. Viable particle candidates need to fulfill several conditions. Firstly, they can interact neither via either the electromagnetic nor the strong force. Instead, they must interact gravitationally in order to explain observational evidence from gravitational lensing effects. Their lifetime must be long compared to the age of the Universe. In order to account for the structure formation of the Universe inferred from the cosmic microwave background, it must be non-relativistic. The only particle already established within the standard model that was considered as a contender, the neutrino, is ruled out by this last point. Additionally, neutrinos are not abundant enough to be a dominant component of DM [3].

A promising candidate is the Weakly Interacting Massive Particle (WIMP). If it does indeed exist, it is predicted to be able to interact gravitationally and via the weak force. Given the typical interaction cross-section and a mass of 100 GeV/c^2 for a weakly interacting particle, todays relic dark matter density turns out to be naturally achieved. This makes the WIMP a strong contender for being the elusive dark matter particle.

1.3 The XENON dark matter search

The XENON dark matter search is based at the *Laboratori Nazionali del Gran Sasso* (LNGS) in Italy. In this underground laboratory, 3600 m.w.e. rock overburden provides shielding against a background introduced by cosmic radiation. It employs a dual-phase time projection chamber (TPC) filled with liquid xenon (LXe), topped by a smaller gaseous phase (GXe). An electric drift field is applied between a cathode located at the bottom of the LXe volume and a gate electrode mounted just underneath the GXe phase. A second, much stronger extraction field is applied between the gate electrode and an anode grid loacted just above the liquid level. Two arrays of a total number of 248 photomultiplyer tubes (PMTs) are mounted at either end of the vessel containing the xenon. A vacuum-insulated double-wall stainless steel cryostat encloses the setup.

A particle entering the LXe phase will produce both excited and ionized atoms. De-excitation of excited molecular states generates a scintillation signal (S1) that is registered by the PMT arrays. A large fraction of the ionization electrons are, in turn, drifted upwards through the electric field, where they are extracted into the GXe phase. There, collisions with the xenon atoms produce a secondary scintillation signal (S2) that is proportional to the number of extracted ionization electrons [11]. The time delay between the S1 and S2 signals, along with the distribution of the S2 light detected by the top PMT array, can be used to reconstruct the 3D location of the interaction site.
Particles interacting weakly predominantly cause recoils of the xenon nuclei (**n**uclear **r**ecoil), whereas charged particles can cause the electrons in the atomic shell of xenon atoms to recoil (**e**lectronic **r**ecoil). This allows a rejection of 99.5% of the γ and β background while retaining 50% of the NR signals [8].

The detection principle is illustrated in fig. 1.1

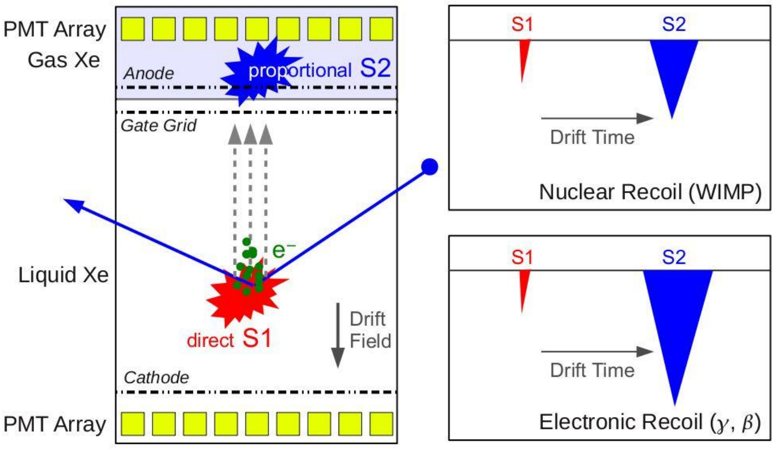

Fig. 1.1 Working principle of the dual-phase xenon TPC employed in the XENON DM search. Figure taken from [8].

As of 09/2019, the detector is undergoing an upgrade from XENON1T with a 2 t LXe [11] taget to its next phase XENONnT, which will increase the active target mass to 6 t [9]. DARWIN is a future ultra-low background DM search project currently in planning whose detection principle will be similar to that of then XENON detectors. It is set to feature a 40 ton dual-phase TPC that will further suppress the background [12].

Chapter 2

Intrinsic radon background in the XENON project and surface coating by electrodeposition

The XENON1T dark matter detector has, at the time of this writing, the lowest background ever achieved among direct DM search experiments. The remaining background rate largely stems from radioactive trace impurities that are inherently present in detector components [10]. Some of these impurities pose a threat to the background level by inducing signals that might mimic those expected for a WIMP interaction.
This chapter details the emanation mechanism of ^{222}Rn, which is the most dominant of these impurities (see section 2.1), and provides a brief overview of currently employed mitigation techniques (section 2.3). The main focus of this work is a study of the applicability of electrodeposited copper coating to mitigate the emanation of ^{222}Rn. An introduction to the principle of electrodeposition given in section 2.4.

2.1 The radon background

For the detection of the hypothetical DM particles (WIMPs), the XENON1T TPC relies on their interactions with the xenon atoms in its active volume (see Ch. 1.3). Despite careful selection of the materials used to construct the detector, it is not currently possible to avoid of some amount of radioactive impurities that might find their way into the LXe volume. The decay of some of these radioactive impurties can lead to energy depositions coinciding with those expected for WIMP interactions. This is the case for certain isotopes from the primordial decay chain of ^{238}U with a half-life of 4.5 Gy. ^{238}U is the most abundant radioisotope found in nature [4] and disintegrates according to the decay chain shown in fig. 2.1.

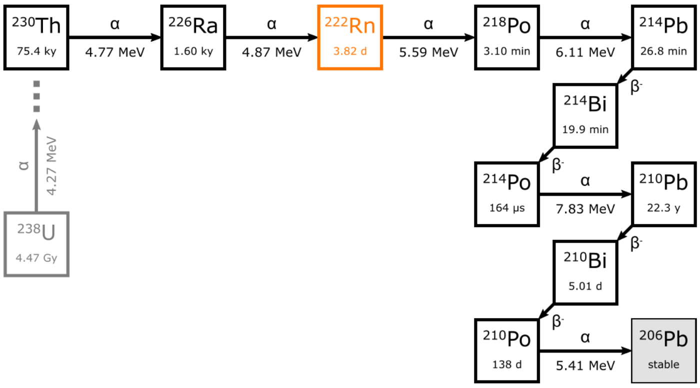

Fig. 2.1 ^{238}U decay chain

With a relatively long half-life of 3.8 d, ^{222}Rn has a chance to distribute evenly within the entire LXe volume. The daughter nuclei of subsequent α decays in the ^{238}U chain all have a discrete recoil energy of several MeV and therefore do not posea direct threat to the low-energy WIMP search region. The electronic recoil (ER) energies from the featured β decays however lie on a spectrum ranging from 0 eV to the respective Q value. This means that it is possible for such a decay to fall into the energy region of interest (ROI) for the WIMP search. Some of these interactions can be discarded if they are accompanied by other events, as is the case for the decay of ^{214}Bi to ^{214}Po: since ^{214}Po has a very short half-life of 164 μs, a detected β decay in the ROI is likely to be immediately followed by signal caused by the α particle of the subsequent decay.

With a half-life of 22.3 years, which is much longer than the expected runtime of the DARWIN detector, the chain effectively stops at ^{210}Pb if only a small number of events is expected. However, the β decay of ^{214}Pb to ^{214}Bi has no associated α event and thereby poses the biggest threat to the background level [11].

Fig. 2.2 shows a projection of the expected energy spectrum of the ER made in 2016.

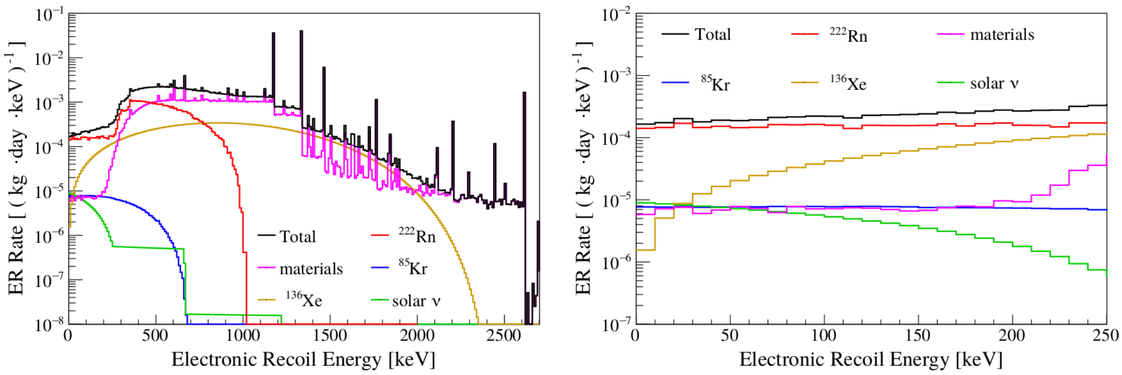

Fig. 2.2 Projected energy spectrum of the separate background contributions for XENON1T with 1 ton fiducial volume. Figure from [11] (2016).

As is evident from fig. 2.2, ^{222}Rn is the largest contributor to the ER rate by far for energies below $\sim$ 100 keV. It constitutes around 85% of the total ER background [11]. Another decay chain containing gaseous radon is that of ^{228}Th (depicted in fig. 2.3), which also contributes to the background but in much smaller quantities.

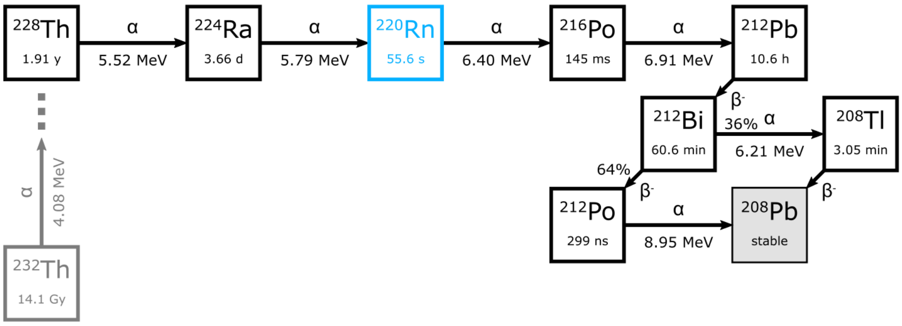

Fig. 2.3 ^{228}Th decay chain

Two processes can be responsible for daughters of the radioisotopes contaminating the detector material reaching the LXe volume. These emanation processes are introduced in section 2.2.

2.2 Emanation processes

Emanation by recoil

When an α particle is emitted as part of a radioactive α decay process, conservation laws dictate that the total momentum of an decay process must be retained. This means that while the majority of the disintegration energy is carried away by the much lighter α particle as its kinetic energy, the daughter nucleus experiences a recoil directed in the opposite direction. Its kinetic energy is given by

$$E_{kin}^{daughter} = Q_\alpha \cdot \left(1 - \frac{M_{daughter}}{M_{mother}}\right) \tag{2.1}$$

where Q_α is the energy remaining after the creation of the decay products, and M_{mother} and $M_{daughter}$ are the mass numbers of the mother and daughter nucleus, respectively [17]. Collisions with its environment transfer its kinetic energy to the substrate material. This means that a daughter nucleus of that chain carrying $E_{kin}^{daughter}$ is able to traverse through the carrier material until all its kinetic energy has been lost to collisions and the nucleus comes to a rest. Subsequent decays may further propel the nucleus within the material. If the site of a ^{226}Ra decay happens to be close enough to the substrate surface, this mechanism might cause ^{238}U progeny to leave the detector material altogether and be released into the surrounding medium.
The recoil energy of β decays is assumed to be negligible due to the large mass of the recoiling nucleus compared to the emitted electron.

The depth a particular daughter nucleus can traverse within a certain substrate material can be simulated using the monte carlo tool SRIM (see Ch. 4.1)

Emanation by diffusion

Being a noble gas, chemical interactions between radon and its surrounding materials are rare. Since it is unlikely to bind to its environment, it is possible for gaseous radon to diffuse through the carrier material until it undergoes a subsequent decay. The diffusion process is thermally driven and dependent on the diffusion constant, which is given by the Arrhenius eq. [16]

$$D(T) = A \cdot \exp\left(\frac{-E}{R \cdot T}\right), \tag{2.2}$$

where A is a constant related to the collision frequency, R is the universal gas const., and T the temperature in K.

Both of these processes contribute to the radon background originating from the detector components. Any attempts to mitigate radon emanation should therefore adress effects from both mechanisms.

2.3 Radon mitigation techniques employed in XENON1T

As mentioned previously, one way to minimize the radon background is by selecting radiopure materials for the detector components. Meticulous screening campaigns are undertaken in order to achieve this [18]. Additionally, the fiducial volume (FV) of the LXe TPC is restricted to the innermost part. Instead of using data from the entire TPC volume, events occuring outside certain boundaries are discarded. This approach serves to reduce the background of cosmic origin as well as that from natural activity due to self-shielding of the xenon.
Cryogenic distillation is another method with which the amount of impurities can be reduced. Using this approach, radon could be continuously removed from the LXe volume by looping the xenon target through a radon removal unit [13].

Despite the unprecedentedly low background of $\sim 10\mu$Bq/kg [11] achieved for XENON1T, future experiments such as the DARWIN dark matter search require an even lower rate of ~ 0.1 μBq/kg [12]. Both the selection of the fiducial volume and cryogenic distillation are actions that can be taken only once the impurities have emanated through the surface into the active volume. An alternative approach is the prevention of surface contaminants reaching the LXe altogether. This could be achieved by depositing a layer of radiopure material onto the emanating surface such that a series of recoiling nuclei would have to traverse a distance exceeding their maximum recoil range (see Ch. 4.1). Ideally, such a layer would be tight enough to prevent any diffusion.
Electrodeposited copper is often used to cover minor imperfections of the substrate material and is popular due to its high plating efficiency [5]. What makes it suitable for our purposes in particular is its natural radiopurity. Previous studies have yielded promising results for the reduction factors achieved when using copper coatings (see [26] and Ch. 4.2).

2.4 Radon mitigation by electrodeposition of copper

Electrodeposition, or electroplating, is an electrochemical process by which a coherent layer of metal coating is deposited onto a conducting surface. The workpiece is submersed in an electrolyte containing ions of the desired material, along with a counter electrode completing the circuit. An electric current flowing through the circuit then causes the ions from the fluid to be reduced onto the surface of the workpiece. Depending on the type of counter electrode used, ions from its surface might dissolve into the electrolyte at a rate equal to the rate of reduction, thereby keeping the ion concentration constant. This is the case when using e.g. a copper electrode when producing a copper coating. A platinum electrode, on the other hand, remains intact throughout the coating process.

Acid copper sulfate solutions are a popular choice for electrolyte [5]. For the coatings produced in the scope of this thesis, copper sulfate dissolved in de-ionized water was employed. Eq. 2.3 describes the reduction process from aqueous to solid copper. Fig. 2.4 shows a schematic of a simple electrodeposition setup and the reduction principle.

$$\mathrm{Cu^{2+}(aq)} + 2\mathrm{e^-} \rightarrow \mathrm{Cu(s)}, \tag{2.3}$$

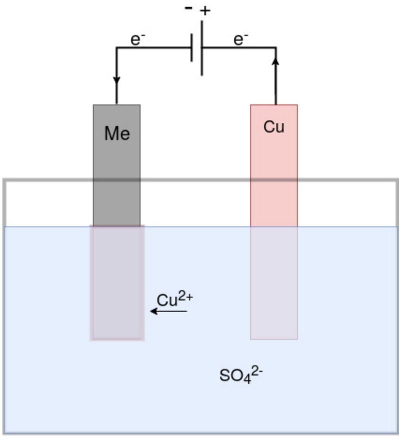

Fig. 2.4 Electrodeposition setup and mechanics. Ions from the electrolyte are reduced onto the surface of the workpiece when a current is applied.

The coating process applied to the samples used in this work is described in more detail in Ch. 3.

In conclusion, the applicability of a coating-based approach to radon mitigation is determined by a number of factors. First and foremost, it is characterized by the reduction factor it yields for the isotopes contributing to the background. Since the emanation process of gaseous radon can occur by both nuclear recoil and diffusion, the coating layer needs to be thick enough to block recoil-induced emanation as well as tight enough to mitigate radon emanating by diffusion. Additionally, the coating should retain its structural properties when employed under operational conditions, i.e. at LXe temperatures. Finally, it should of course not distort detection signals nor introduce additional background.

Ch. 3 will provide an overview of the methods used to test these parameters.

Chapter 3

Experimental setups, samples and methods

In the previous chapter, a number of parameters were identified as a figure of merit for coating-based approaches to radon mitigation. Several methods were devised as a means to quantify these: A Monte Carlo simulation tool was employed to obtain the maximum recoil range expected of the relevant isotope chain. The minimum thickness of the coating layer deposited on the samples necessary to mitigate all emanation by recoil was determined based on this result. Thoriated tungsten welding rods were coated by electrodeposition of copper, their activity in several isotope channels measured before and after, and the reduction factor determined. Finally, their was measured as a function of temperature in order to both test the reduction factor close to operational temperatures and to gain a deeper understanding about the contributions of diffusion and recoil to the emanation.

This chapter details the specifics of the samples, detectors and setups utilized; the results of these procedures are presented in Ch. 4. Several of the parameters mentioned above are yet to be explored or have results still in the pipeline, a brief review of which is to be found in Ch. 5.

3.1 Samples

The ultimate goal of our studies towards radon mitigation serves the purpose of reducing the radon background expected in the planned DARWIN dark matter detector. As such, an ideal sample to conduct research on should mimic both the surface properties and origin of emanation of the detector materials contributing to the background level. The former is important since coating layers may behave differently when applied to different substrates. The detection of the relevant isotopes using more conventionally available methods should also, of course, remain feasible; since the materials used for low-background searches are selected for their radiopurity, we expect their inherently low emanation rate to be negligible in data taken by tabletop-detectors. Studying the materials whose emanation reduction we target would therefore not be particularly practical. Instead, we are looking for materials that produce sufficient activity to be able to determine even potentially high reduction factors. Two sample types, introduced below, were found that satisfy above requirements to varying degrees.

3.1.1 ISOLDE sample

The ISOLDE sample is one of two square X2CrNiMo18-14-3 (1.4435) stainless steel plates of 20 mm width and 1 mm thickness that were implanted with ^{226}Ra at the **I**on **S**eparation **O**n-**L**ine **De**vice (ISOLDE) at CERN in 2017. A total number of $N = 5 \times 10^{11}$ ^{226}Ra ions were impinged on an area of 5 × 5 mm [15], which, according to the law of radioactive decay (eq. 3.1), should correspond to an activity of approx. $A_{^{226}\mathrm{Ra}} = 6.9$ Bq. The law is given by

$$A = \lambda \cdot N, \tag{3.1}$$

where λ denotes the decay constant of the isotope.
Since the site of implantation is close enough to the surface of only one side of the plate for nuclei to be able to recoil through (see Ch. 3.5), a maximum of half the ^{222}Rn decays is expected to be detected.

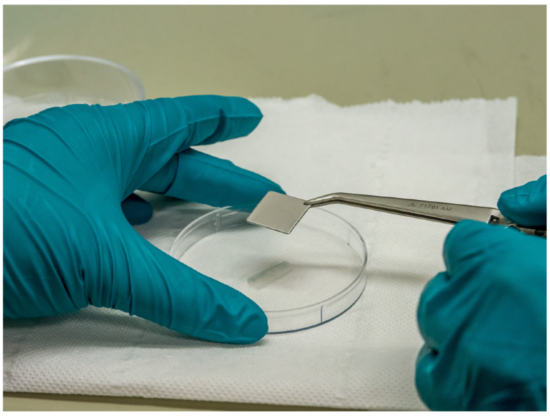

Fig. 3.1 Stainless steel sample implanted with ^{226}Ra at the ISOLDE facility [15]

Implantation mechanism

The ISOLDE facility produces radioactive isotopes using target fragmentation, spallation and fission reactions [19]. A charged particle beam from a particle accelerator is directed at a target, where the nuclides are ionized and released from the target material via diffusion. In order to isolate the desired isotope from the numerous possible reaction products, they are accelerated and separated by mass using magnetic dipole mass separators. The resulting radioactive ion beam (RIB) is then directed towards the sample that is to be implanted, where the incident ions penetrate the sample surface. Through collisions with the target material, the ions lose their kinetic energy until they come to a rest within the sample [20, 21]. In our case, a 1 GeV proton beam was aimed at a depleted ^{238}U target to produce the RIB. The expected mean implantation depth is (8.47 ± 2.24) nm [26].

3.1.2 Thoriated welding rods

In addition to the ISOLDE sample, it was found that thoriated tungsten welding electrodes of type WT-40 emanate sufficient radon to fulfill our detection requirements. The welding electrodes have a diameter of 4.8 mm, are 17.5 cm long and contain 4% ThO_2 dispersed throughout the electrode during manufacturing. The majority of their activity originates from emanation of ^{220}Rn, however some small fraction of ^{222}Rn most likely produced by trace impurities introduced during the manufacturing process is also present. As will be shown in Ch. 4.1, these two isotopes have different maximum recoil ranges and might not have the same diffusion coefficients in copper either. Previous studies have hinted that resulting reduction factors can differ by as much as a factor of ten [26]. This is why these samples are examined for both radon isotopes, using a radon monitor as well as miniaturized proportional counters (see section 3.2).

A total of 61 rods were investigated during the course of this study. The samples stem from two separate batches that were not produced by the same company, the second of which shows double the ^{222}Rn activity as the first (around 0.13 μBq and 0.07 μBq per rod, respectively). Their ^{220}Rn activity averages approx. 13 mBq/rod (see Ch. 4.3).

3.2 Detectors

The reduction factor achieved by any given mitigation technique is one of the defining characteristics that determine its suitability. Since the two decay chains whose reduction factors are examined decay by production of primarily α radiation, several detectors capable of providing information about these decay channels were employed and are introduced below.

3.2.1 Radon monitors

The detection principle of radon monitors relies on radon progeny decaying on a silicon PIN diode mounted to the top of the detector. As gaseous radon reaches the detector volume, either by diffusing through the carrier material or by recoiling beyond its surface, its predominantly positively charged [27] daughters are drifted towards the diode by application of a negative high voltage field between diode and vessel. In a subsequent α decay occuring directly on the diode, the emitted α particle can transfer energy its energy to the diode substrate. There, it creates a number of electron-hole pairs proportional to the energy deposited on the diode in the depletion region of the semiconductor material. A reversely biased voltage applied to two electrodes of the diode separates the charges. This creates a flow of current between anode and cathode that can then be amplified and read out [24].

Both monitors used to measure our samples feature a gas in- and outlet through which ambient air can be evacuated and N_2 be filled in its stead. Fig. 3.2 shows a schematic of a radon monitor and its working principle.

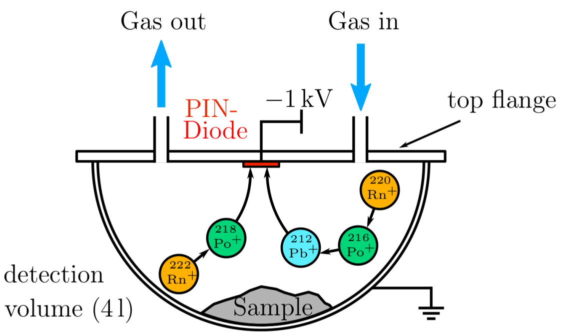

Fig. 3.2 Schematic and detection principle of a radon monitor. An electric field is applied that drifts positively charged radon daughters towards the diode.

Determination of sample activity

This section is meant to provide an overview of the origin and effects that are expected to influence the shape of each peak found in the energy spectra taken with the radon monitors. Fig. 3.3 shows an example of a typical spectrum of a thoriated tungsten welding electode. The isotope signals from the ^{220}Rn chain are indicated in blue, the ones from the ^{222}Rn in orange (see fig. 2.1 and 2.3 for full decay chains).

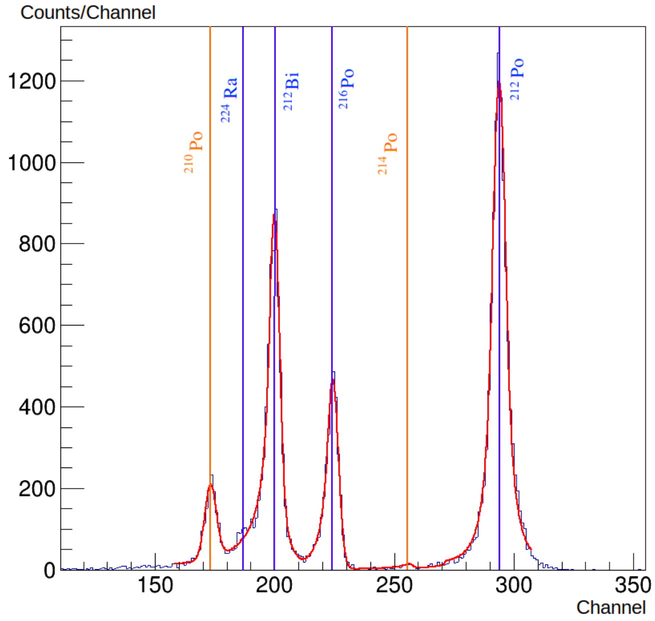

Fig. 3.3 Typical spectrum of a thoriated tungsten welding electrode. Isotopes from the ^{220}Rn chain are labeled in blue, from the ^{222}Rn chain in orange. Data taken from measurement of 31 coated rods.

As the thoriated welding electrodes do contain trace amounts of isotopes from the ^{238}U chain, some small number of signals from that subsequent decays is expected. Additionally, the length of the half-life of ^{210}Po (138 d) makes it possible for a diode to be contaminated for some time after the detector has housed a sample emanating sufficient quantities of ^{222}Rn. This means that not all signals seen in a spectrum must necessarily stem from the sample in the detector at the time. Since ^{218}Po has a recoil energy very close to that of ^{212}Bi and the half-life of ^{210}Po is quite long, it is easiest to use ^{214}Po to obtain information about the amount of ^{222}Rn present in a thoriated welding rod. Since ^{220}Rn is neutral, it will not be affected by the drift field and is therefore expected not show up in the spectrum in significant quantities. The different peak heights for isotopes of the same decay chain are, in part, caused by the drift time necessary for a daughter nuclide to reach the diode. This leads to a lower detection efficiency for progeny early in the decay chain, especially for a short-lived isotopes like ^{216}Po with a half-life of 145 μs. Branching ratios also play a role, e.g. in the case of ^{212}Bi that undergoes α decay only 36% of the time.

Rather than the delta functions we would see if the energy of each α particle were deposited and detected in its entirety, several effects contribute to the broadening of each peak: given that the detectors used have a finite resolution, gaussian wings towards both higher and lower energies are generally expected. Since decays are bound to occur in every direction, many recoils will not be directed perpendicularly towards the diode surface. This means that the decay products will traverse a longer path within the diode substrate before being collected. Statistical fluctuations during detection further exacerbate the tailing towards lower channels.

The general shape of an average signal peak is best described using the Crystal Ball function that was developed by the Crystal Ball Collaboration [29],

$$f(x;\alpha,n,\overline{x},\sigma) = N \cdot \begin{cases} A \cdot (B - \frac{E-\mu}{\sigma})^{-n}, & \frac{E-\mu}{\sigma} \leq -\alpha \\ \exp(-\frac{(E-\mu)^2}{2\sigma^2}), & \frac{E-\mu}{\sigma} > -\alpha, \end{cases} \tag{3.2}$$

where $A = (\frac{n}{|\alpha|})^n \cdot \exp(-\frac{|\alpha|^2}{2})$, $B = \frac{n}{|\alpha|} - |\alpha|$, N is a normalization factor and α, n, $\overline{x}$ and σ are fit parameters.

Additional tailing towards higher energies, in turn, might occur due to coincidence counting of preceding decays: if an isotope has a particularly short half-life $\mathrm{T}_{1/2}$ (as is the case for ^{212}Po, where $\mathrm{T}_{1/2}$ = 299 ns) the detector might not be able to resolve the signals separately, causing energy overflow from one signal to contribute to the next. In this case, a double-sided Crystal Ball function can be employed to describe the peak shape.

Ingrow function

If a radioactive decay is followed by another with a much shorter half-life, the quantity of the first isotope will eventually grow constant as its rate of production will equal that of its decay. This state is known as a *secular equilibrium*. This means that for the signal recorded by a detector without previous contamination, an ingrow function can be defined from which the equilibrium activity can be determined.

The ingrow function of ^{212}Po has proven to be the most reliable indicator for the sample activity of the thoriated tungsten welding rods as it is preceded by isotopes of relatively short half-lives and its energy is sufficiently separated from its neighbouring peaks to allow clear signal distinction. It was shown in [30] that the ingrow function of ^{212}Po is

$$\begin{aligned} A^{ingr.}_{^{212}\mathrm{Po}} = A^{eq.}_{^{216}\mathrm{Po}} \lambda_d [& \frac{\lambda_c}{(\lambda_b - \lambda_c)(\lambda_d - \lambda_b)} \cdot (e^{-\lambda_b t} - e^{-\lambda_c} t) \\ & + \frac{\lambda_b}{(\lambda_b - \lambda_c)(\lambda_c - \lambda_d)} \cdot (e^{-\lambda_c t} - e^{-\lambda_d} t) + \frac{1}{\lambda_d}(1 - e^{-\lambda_d t})], \end{aligned} \tag{3.3}$$

where $\mathrm{A}^{eq.}_{^{216}\mathrm{Po}}$ is the equilibrium activity of ^{216}Po, and λ_b, λ_c, and λ_d are the decay constants of ^{212}Pb, ^{212}Bi, and ^{212}Po, respectively. It was assumed that ^{216}Po is in equilibrium with ^{220}Rn due to its short half-life of 145 μs, i.e. that $\mathrm{A}^{eq.}_{^{220}\mathrm{Rn}} = \mathrm{A}^{eq.}_{^{216}\mathrm{Po}}$.

3.2.2 Alpha spectrometer

An alpha spectrometer functions in much the same way as the radon monitors introduced in section 3.2.1. The defining difference between the two is the lack of high voltage applied to the alpha spectrometer. Instead, it is operated under vacuum conditions, thereby avoiding collisions between decay products and ambient particles, and relies on close proximity between diode and sample to ensure sufficient detection efficiency. It should be noted that since no drift field is applied, only decays directed directly at the diode can be detected. One advantage of this approach is the possibility of detecting activity from neutral isotopes such as ^{220}Rn. Figure 3.4 shows a schematic of an alpha spectrometer.

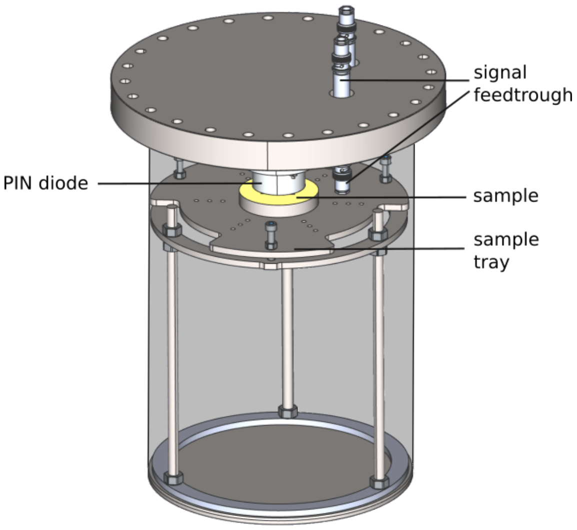

Fig. 3.4 Schematic of the alpha spectrometer [28]. Samples are placed close to the diode for detection of α decays.

3.2.3 Miniaturized proportional counters

Miniaturized proportional counters are ionization detectors that were developed for the detection of ^{71}Ge in the search for GALLEX solar neutrino experiment at the MPIK in Heidelberg. Since the experiment relied on a high detection efficiency, low and time-stable background and good radiopurity [31], they were adapted to use for our study of radon emanation. The counters feature a small chamber of around one cm^3 containing an inert counting gas that is ionized by particles entering the chamber, which produces a number of electron-ion pairs proportional to the energy deposited by the particle. An electric field separates the pairs and accelerates them towards anode and cathode, where a current is produced. This current is then amplified and can be read out to provide information about the energy of the ionizing particle.
Due to their low threshold (< 0.5 keV) [31] compared to the recoil energy of ^{222}Rn ($E_{recoil} = 5.59$ MeV, see table 2.3), the counters go into saturation when used for ^{222}Rn measurements and yield no information about the energy of the event. Because of the low background rate, however, it is valid to assume that every event registered is caused by ^{222}Rn.

In order to measure the ^{222}Rn content of the thoriated welding rods, they are placed inside a vacuum-tight emanation vessel (depicted in fig. 3.5) for several days. This allows the number of radon atoms within the vessl to reach an equilibrium. The radon gas can then be extracted and filled into the counters along with the counting gas.

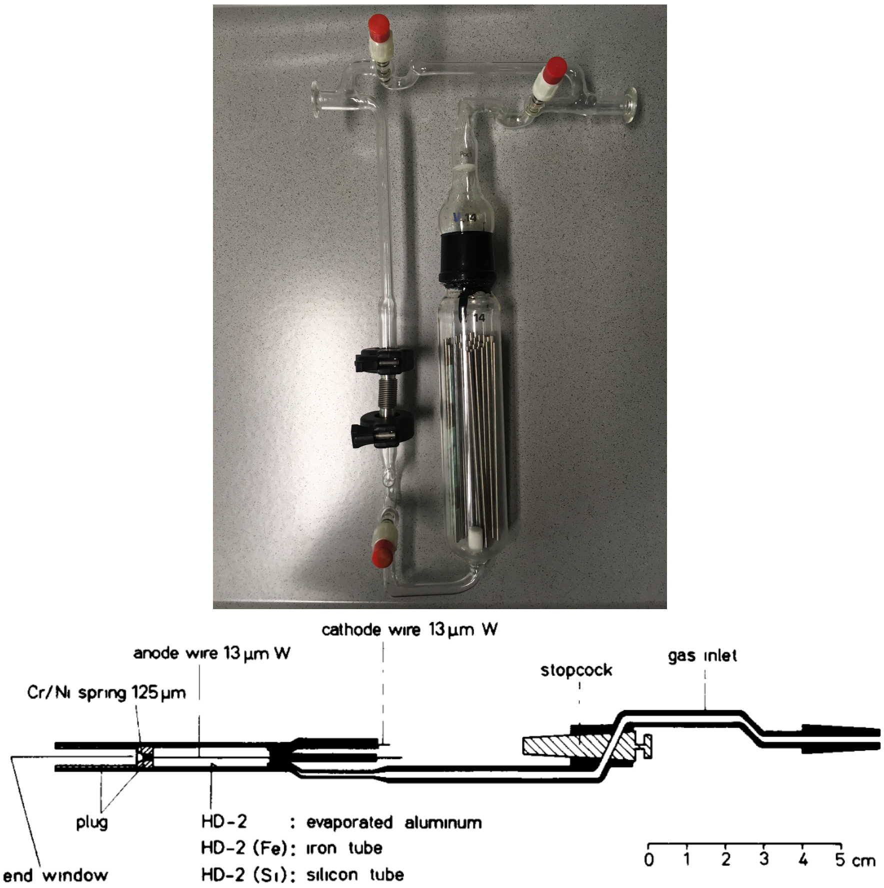

Fig. 3.5 *Top:* Thoriated tungsten welding rods before being connected to the miniaturized proportional counters. *Bottom:* Schematic of miniaturized proportional counters [31]

3.3 Coating setups

As introduced in section 3.1, welding rods and square stainless steel plates were used to study the properties of electrodeposited copper coating. These sample types have different geometries that need to be taken into account when designing the setups to coat them. The setups constructed for this purpose are described in sections 3.3.1 and 3.3.2. Several considerations that are relevant to the coating procedure in general will be discussed in the section below.

3.3.1 Multi-slot electrodeposition setup

Since the ^{222}Rn-yield of the thoriated welding rods used is low, large sample sizes are needed in order to maximise the sensitivity of the reduction factor. Coating a large number of rods, in turn, tests the reliability of the method used, but also requires a system capable of coating samples with high consistency while simultaneously minimizing runtime and changes to the system. This was achieved using a custom-built multi-slot electrodeposition setup suited for coating up to five rods in parallel.

The setup consists of a 5 L glass beaker with a diameter of 25 cm in which two copper electrodes are immersed, one lining the beaker and one in the center such that the rods are coated as evenly as possible. The central electrode is a cylindrical, solid piece of copper

with a diameter of 5.5 cm and a height of 9.5 cm, whereas a 2 mm copper sheet of 13 cm height serves as the outer ring. A DC power supply providing a current of up to 40 A was used and connected to the PC via a power supply controller (see fig. 3.6). The sample rods were connected to the power supply with alligator clips. Bath temperature and agitation were maintained by a heating plate with a magnetic stirrer. A PVC plate placed on top of the container and centered by a shallow indentation fitting the rim of the beaker functions both as holder for the rods to ensure even spacing, and as a lid for reducing evaporation of the electrolyte. A 0.5-molar $CuSO_4$ solution prepared by dissolving copper(II) sulphate pentahydrate in 1-molar sulphuric acid serves as electrolyte.
Figure 3.6 below shows a schematic of the setup.

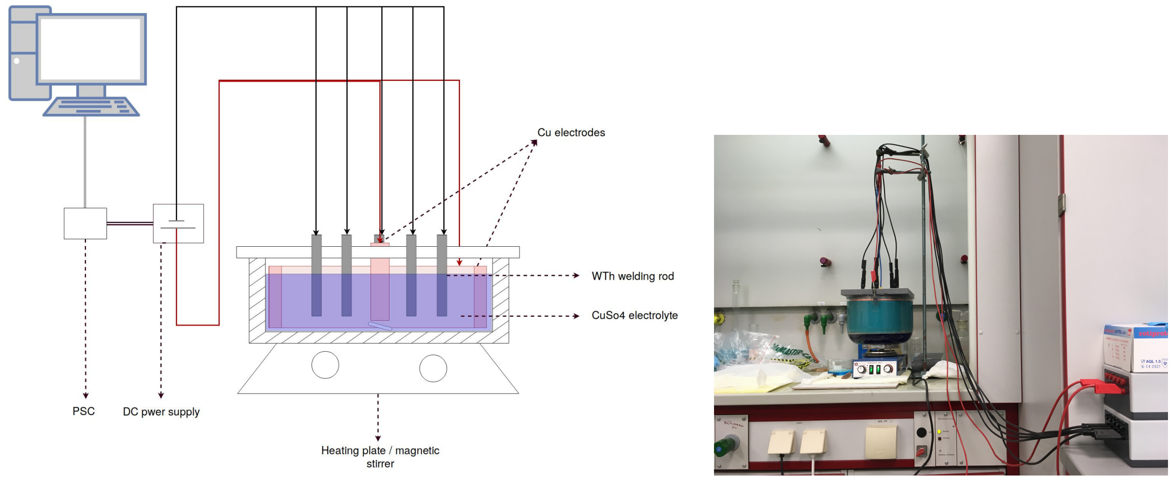

Fig. 3.6 Multi-slot coating setup used for electrodepostion of copper on tungsten welding rods, as well as stainless steel tubes and rods

Sample surface pre-treatment

Any contaminants (e.g. grease) residing on the sample surface might compromise adhesion between the coating layer and the substrate. It is therefore imperative that the samples are cleaned thoroughly before undergoing the coating process [22]. This was done by dipping the tips of the rods in acetone in order to dissolve paint marks applied by the manufacturer and subsequently wiping each rod with isopropanol-soaked precision wipes. Gloves were worn when handling the samples in order to prevent surface contamination.

Real-time process control

A power supply controller of type 232 EXT (Delta Elektronika) is employed to translate voltage and current settings from the PC to the SM1540-D (Delta Elektronika) power supply. After providing the surface area expected to be coated, an interface outputs the surface current density and uses this data to calculate the total mass m_{Cu} (eq. 3.2) and thickness d (eq. 3.3) of the coating layer deposited on the workpiece in real-time. This is done by considering the reduction reaction it undergoes: by virtue of the reduction process

$$* \, \mathrm{Cu}^{2+}(\mathrm{aq}) + 2\mathrm{e}^{-} \rightarrow \mathrm{Cu}(\mathrm{s}), \tag{3.4}$$

the number of copper ions N_{Cu} reduced is directly dependent on the the total number of electrons transported from the copper electrodes to the rods. Consequently, an integration of the current $I(t)$, divided by the number of electrons needed to solidify one copper atom, yields

$$N_{Cu} = \frac{1}{2e} \int_{t_1}^{t_2} I(t)dt = m_{Cu} \cdot \frac{N_A}{M_{Cu}}, \tag{3.5}$$

where $\mathrm{N_A}$ is Avogadro's constant and t_1 and t_2 are the start and end times of the process, respectively. Knowing the density $\rho_{Cu(s)}$ of solid copper then allows an estimation of the coating layer thickness d,

$$d = \frac{m_{Cu}}{\rho_{Cu(s)} \cdot A}. \tag{3.6}$$

This approach merely provides an approximation of the deposited coating thickness since it relies on the assumption that the density and thickness of the layer are uniform and not dependent on experimental conditions. It should, however, be a sufficiently accurate parameter for gauging the coating duration needed in order to achieve relatively similar layer thicknesses. It is worth noting that the coating process is started and stopped manually, which may introduce further slight inconsistencies.

Coating procedure

As several studies [5, 23] as well as some evidence from the consistency tests in the next section have shown, an increased bath temperature leads to higher conductivity and decreased viscosity and surface tension of the electrolyte. In the interest of maintaining consistent coating parameters for meaningful results it is therefore important that the bath temperature be kept as uniform as possible across all coating runs. This was accomplished by turning on the magnetic heating plate and stirrer several hours before the coating process was started. Additionally, bath temperatures were monitored throughout the course of all measurements; they were kept in the range of roughly (45 ± 5)°C. The electrolyte was kept in constant agitation when in operation, both as a means of keeping the temperature throughout the fluid homogeneous and in order to avoid ion depletion (see section 3.3.1).

Once cleaned, the samples were subdivided into batches of up to five pieces. Since the area surrounding the crocodile clamp connection was left blank, each batch was coated from both sides such that the entirety of each rod could be exposed to the electrolyte. This means that the middle section of each rod has a double layer of coating, whereas its ends are coated only once. Since the rods have a length of 17.5 cm and the area coated for each step is around 11.5 cm long, this leaves 5.5 cm of overlap on each rod. The implications of this should be taken into account when considering the reduction factor achieved by a certain coating thickness.

The result is visualised in fig. 3.7. The figure shows a clearly visible drop from the initial surface current density to a constant final value during the first ∼ 50 s of runtime. This is likely caused by the differing electrochemical properties of copper and tungsten. The surface current density drop seen between 0 and 50 s runtime can be identified, then, as the period during which tungsten is slowly replaced by copper as the surface on which the reduction process takes place. This also explains the difference between the initial surface current densities of steps one and two: since the majority of the surface is already covered by a layer of copper, the starting current density is much closer to the final value. As can be seen in fig. 3.9, where all coatings were conducted using the same voltage settings, slight environmental changes like temperature can have an impact on the surface current density. The differene between the current densities of step 1 and 2 seen in fig. 3.7 is most likely caused by such fluctuations.

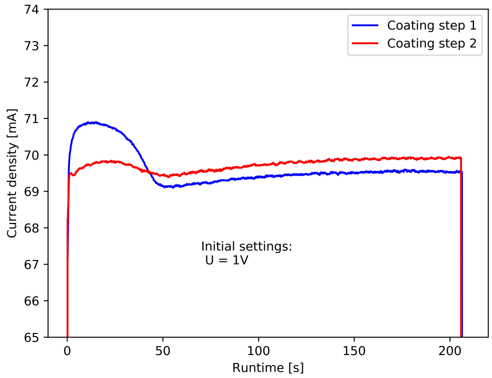

Fig. 3.7 Sample surface current density of a typical two-step coating process. The steps refer to the coating of each side.

Consistency of coating process

In order to ensure an even spread of the coating among the samples and to rule out inconsistencies caused by the setup itself, the mass of each rod was monitored throughout the coating process. Additionally, the surface current densities applied were tracked to verify comparability of experimental conditions across coating runs.

Mass distribution and surface current density: The mass distribution between rods coated in the same batch was monitored by weighing each sample before and after coating, as well as between coating steps one and two. Fig. 3.8 below shows a histogram of the mass increases during the first and second step of the coating of 31 thoriated tungsten welding rods separately. These data points excluded for the improved fit are due to procedural errors. As is evident from the plot, both steps produce a Gaussian-shaped distribution with an average total mass increase of (177.2 ± 3.4) mg for a target coating thickness of 5000 nm. This is reasonably consistent with the masses approximated by the process control according to 2.3, which yielded an average mass increase of Δm = (169.2 ± 0.5) g. It should be noted that the two distributions are slightly shifted despite having been coated using identical settings. This likely stems from the previously mentioned difference between the properties of tungsten and copper and the resulting difference in surface current density of (69.3 ± 0.9) mA/cm^2 for step one, and (69.9 ± 0.7) mA/cm^2 for step two.

Stirring: The concept of copper electrodeposition relies on the presence of Cu^{2+} ions in the area immediately surrounding the cathode to maintain current flow (c.f. Ch. 2). As the number of ions in the surrounding electrolyte decreases, the resistance rises gradually until the deposition process can no longer take place. This can be seen in fig. 3.9, which shows the surface current density recorded during a coating run where the stirrer was not turned on during the first minute (red). The current densities of the other batches are shown for comparison (gray), where the 2nd coating step is presened as a dotted line. After starting at value similar to that of the other coating procedures, the surface current density shows a noticably deeper drop than that of all coating procedures with

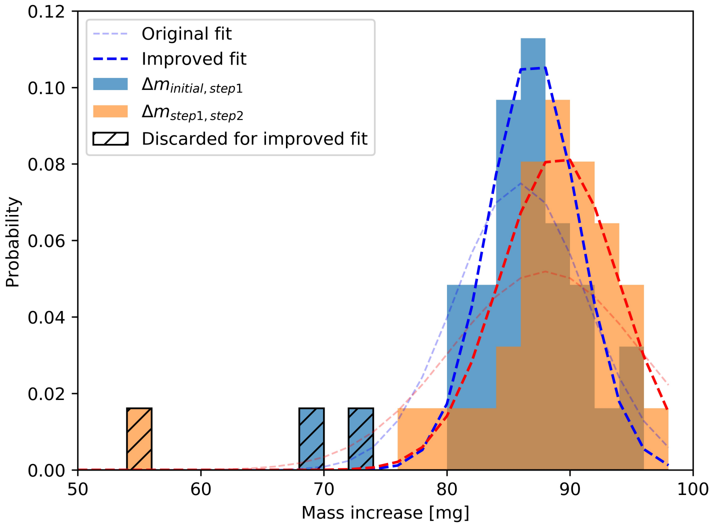

Fig. 3.8 Mass incease of the coating layer between each step measured for 31 thoriated welding rods. The outliers excluded from the fit are due to procedural errors.

an active stirrer. A slow incline can be seen after around 70 s runtime. A similar slope is present in some of the other coatings as well; it is not entirely clear what causes this phenomenon. It is possible that the drop in ion concentration becomes secondary to this effect after the 70 s mark.The stirrer was turned on just after 100 s runtime, followed by an immediate increase back to the initial surface current density. This shows that it is of utmost importance to the continued success of the deposition that constant agitation of the electrolyte take place. It is worth noting that the initial surface current density of the concerning batch is slightly higher than that of the other batches since this batch comprised of three rods rather than five, and the voltage settings was adjusted accordingly. An imperfect adjustment led to a higher surface current density than intended.

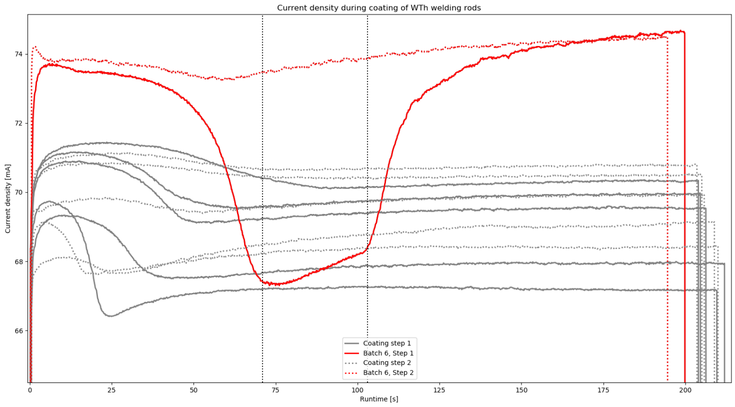

Fig. 3.9 Drop of surface current density (red) due to ion depletion. Stirrer was off until 100 s runtime, then turned on. The surface current densities of other coating runs are dipayed in gray.

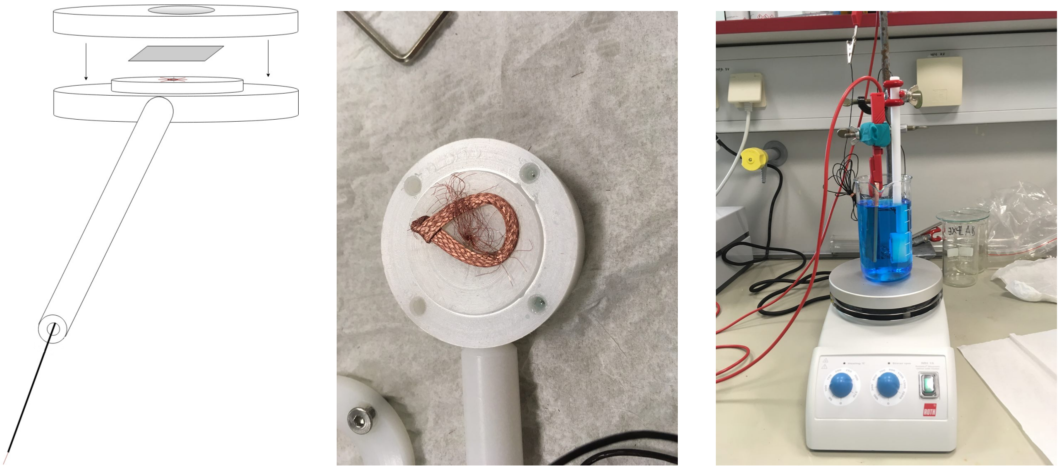

Fig. 3.10 *Left:* Schematic of HDPE sample holder. *Middle:* Wire connection between plate and power source. *Right:* Coating setup for ISOLDE sample.

3.3.2 ISOLDE sample holder and bath

In order to prevent damaging the implanted area of the ISOLDE-implanted stainless steel plate, a HDPE (high-density polyethylene) sample holder was used to connect the sample to the power supply. The holder was immersed in 300 mL of 0.5 M/L $CuSO_4$+ 1 M/L H_2SO_4 electrolyte along with a copper counter electrode and connected to the same power supply setup that was used for the thoriated tungsten welding rods. A ring with a circular cutout 19 mm in diameter is used to keep the sample in place while providing access to the site of implantation. Fig. 3.10 below shows holder and setup. A thin wire with its strands fanned out, against which the plate is pressed by the holder, connects it to the power source. A piece of de-soldering braid was placed between the holder and wire strands in order to generate a higher pressure to improve the connection.

Consistency tests and impact of sample holder

The ISOLDE sample holder covers a considerable fraction of the plates and prevents electrodeposition from taking place where it touches the sample (see fig. 3.13). This means that if the site of implantation was blocked by the holder, the reduction factor caused by the coating would be skewed as not the entire emanating area would be covered. At the same time, the holder blocking the site of implantation would also reduce the amount radon emanation detected by an alpha spectrometer (see section 3.2.2). This is why the sample spectrum of the ISOLDE sample was measured with and without the top holder ring. Fig. 3.11 shows this setup.

Fig. 3.11 ISOLDE sample and holder in alpha spectrometer for determining potential reduction factor caused by holder. *Left*: with top holder ring, *right*: without top holder ring

The resulting spectra and their residuals, which are defined as

$$Res = \frac{A_{with} - A_{without}}{A_{with} + A_{without}}, \tag{3.7}$$

are shown in fig. 3.12 below.

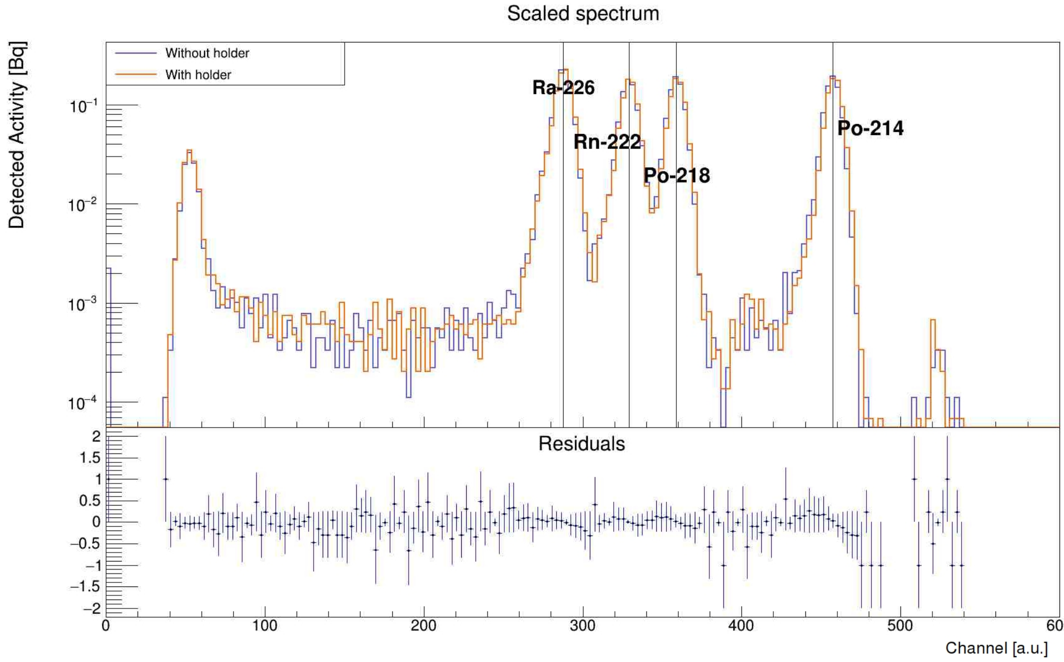

Fig. 3.12 Spectra and residuals of ISOLDE sample with and without top holder ring measured in alpha spectrometer. Scaled by runtime.

Table 3.1 summarizes the detected activities and resulting reduction factor found for each isotope, where

$$\mathrm{R} = \frac{\mathrm{A}_{without}}{\mathrm{A}_{with}}. \tag{3.8}$$

The activities of ^{214}Po, ^{218}Po and ^{222}Rn deviate significantly from that of ^{226}Ra due to ingrowth effect.

	$A_{without}$ [mBq]	A_{with} [mBq]	R
^{226}Ra	$(990 \pm 11_{stat})$	$(984 \pm 8_{stat})$	1.01 ± 0.01
^{222}Rn	$(751 \pm 9_{stat})$	$(741 \pm 7_{stat})$	1.01 ± 0.02
^{218}Po	$(762 \pm 9_{stat})$	$(740 \pm 7_{stat})$	1.03 ± 0.02
^{214}Po	$(750 \pm 9_{stat})$	$(741 \pm 7_{stat})$	1.01 ± 0.02

Table 3.1 Reduction factors found in spectra taken of ISOLDE sample with and without top holder ring. Data taken using alpha spectrometer.

Table 3.1 shows that all detected activities with the sample holder are compatible with those without.

A number of blank (i.e. unimplanted) samples of the same geometry and make as the ISOLDE plate were coated in order to determine whether the coating process using the sample holder produces reliable results. It was found that a using an initial surface current density of 100 mA/cm^2 with a reduction to 10 mA/cm^2 after 1 μm reliably produces a stable-looking coating layer that does not rub off using precision wipes. This coating does not, however, pass the scotch tape test (see section 3.6). It was found that when the coating pulls off easily when removing the tape. No further testing has been conducted at this stage since the reduction factors measured for the thoriated tungsten welding rods are not sufficiently high, nor understood well enough, to warrant a coating of the ISOLDE sample itself (see Ch. 4.3).
Fig. 3.13 shows one coated sample produced using the parameters above.

Fig. 3.13 Stainless steel plate coated using the HDPE sample holder.

3.4 Measurement of the temperature dependence of radon emanation

As mentioned in section 2, radon and its progeny can emanate either by nuclear recoil or by diffusing through the carrier material. In order to identify the dominant process, the temperature dependence property described by eq. 2.2 can be harnessed: diffusion-driven emanation would show a clear correlation with the sample temperature, while a recoil-driven process would not. A measurement of the activity emanating from samples of a range of temperatures would also double as a pointer towards the behaviour and integrity of an electrodeposited layer of copper coating when the sample is placed in temperatres similar to those at which the DARWIN cryostat is set to operate.

For this purpose, a gas circulation loop was built around a radon monitor such that the emanation vessel containing ten thoriated tungsten welding rods could be immersed in a thermal bath. The system was filled with N_2 that was circulated with a small piston pump while the flow rate was controlled with a mass flow controller (MFC). The temperatures of both the inside of the emanation vessel and the surrounding cooling fluid, as well as the pressure inside the monitor, were tracked throughout each measurement run using two PT100 temperature sensors. The thermal bath was cooled using a HAAKE EK 90 immersion cooler submersed in Novec^{TM} cooling liquid. The fluid was selected for its non-flammable and dielectric properties; one downside, however, is its extreme volatility. Several layers of heavy-duty aluminium foil were wrapped around the Dewar opening and any instruments protruding from it to counteract the diffusion of the fluid. This solution also prevented the formation of a layer of ice through condensation of ambient moisture. A magnetic stirrer was placed underneath the Dewar containing the fluid for the sake of maintaining a uniform temperature throughout the bath.

The system is shown in fig. 3.14 below and is capable of cooling down to temperatures as low as −90°C.

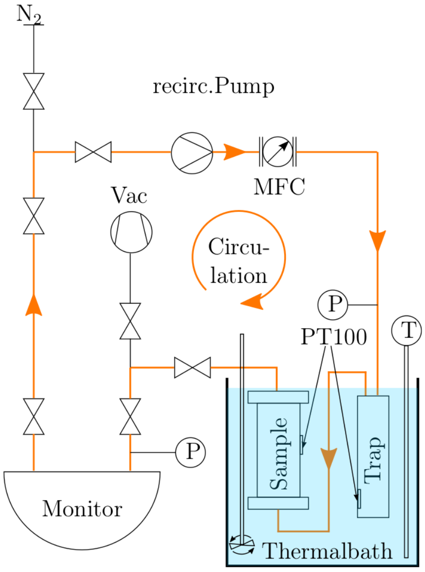

Fig. 3.14 Schematic of the recirculation system for measuring the temperature dependence of the activity of the thoriated tungsten welding rods.

As with other radon monitor measurements, each spectrum was taken for three days in order to give the ^{212}Po isotope sufficient time to grown in. The activity was then obtained by fitting the ingrow function eq. 3.3.

3.5 Simulation of recoil range using SRIM

SRIM (**S**topping and **R**ange of **I**ons in **M**atter) is a tool for simulating interactions between ions and matter using the Monte Carlo method BCA ([B]inary **C**ollision **A**pproximation). This approach is based on the assumption that the interactions of energetic projectiles can be separated into a series of distinct two-body encounters [35]. The program uses the recoil energy and ion type as well as the material of the desired target layer(s) and outputs a simulated recoil range distribution of the ions within the substrate. Within the scope of this thesis, it is used to approximate the recoil range of the progeny from the ^{238}U and ^{228}Th chains.

3.6 Scotch tape test

The scotch tape test is a widely used qualitative method to test the adhesiveness between a coating or paint layer to a substrate. The test is conducted by applying pressure-sensitive tape to a coated substrate area where it is pressed firmly to the surface. The bond is considered adequate if no coating residue is left on the tape after it is pulled off [33]. Original Scotch™ tape was used to test the samples coated in this work.

In this chapter, the methods used in this work were introduced. The results of these procedures are presented in Ch. 4

Chapter 4

Results of coating suitability investigation

In this chapter, the results obtained using the methods introduced in Ch. 3 are presented. In section 4.1, an estimation is made for the minimum coating thickness required to mitigate all recoil-driven activity from the ^{238}U and ^{228}Th chains. Section 4.2 gives a brief overview of the reduction results that were previously achieved using electrodeposited copper. In sections 4.3 and 4.4, these results are compared with the reduction factors and structural properties of the samples coated within the scope of this thesis. Finally, in section 4.5, the temperature dependence of ^{212}Po activity of coated thoriated tungsten weldin rods is investigated. An overview of the findings is given and their implications are discussed in section 4.6.

A number of scanning electron microscope (SEM) images were taken at the Electron Microscopy Core Facility of Heidelberg University. These are shown in appendix A.

4.1 Recoil Range

As mentioned in section 3.5, the tool SRIM (**S**topping and **R**ange of **I**ons in **M**atter) uses Monte Carlo Methods to simulate interactions between ions and matter. It can be used to approximate the probability distribution with which a decay product with a given nuclear recoil energy $E_{recoil} \equiv E_{kin,\ daughter}$ (see eq. 2.1) is expected to reach a certain depth within a material. Fig. 4.1 shows what a typical output diagram looks like for the decay of ^{226}Ra to ^{222}Rn, where the trails in red are the simulated paths of ^{222}Rn nuclei with a recoil energy of 86.2 keV in copper (density: 8.92 g/cm^3), projected onto a lateral plane. Each black dot represents the end point of one ion.

A total of 20 000 decays were simulated for each isotope.

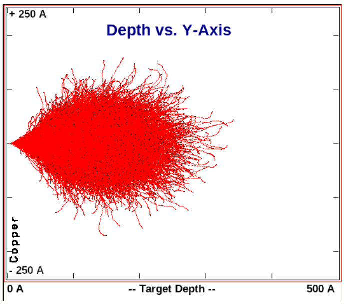

Fig. 4.1 SRIM simulation of ^{226}Ra decay.

For the decay chains of ^{238}U and ^{228}Th (see Ch. 2.2), the simulation yields the mean and maximum recoil distances listed in tables 4.1 and 4.2 as $< d >$ and d_{max}, respectively. Here, d_{max} refers to the distance at which 99% of the ions are stopped. The error of the mean recoil distance is defined by SRIM as the square root of the variance (straggling),

$$\sigma \equiv \Sigma\sqrt{(\Delta x_i)^2}, \tag{4.1}$$

where x_i is the projected range of ion i on the axis pependicular to the target surface [34].

Mother isotope	Daughter isotope	Half-life	E_{recoil} [keV]	$< d >$ [nm]	d_{max} [nm]
^{226}Ra	^{222}Rn	1600 y	86.2	13.7 ± 4.3	26.0
^{222}Rn	^{218}Po	3.8 d	100.7	15.2 ± 4.9	29.0
^{218}Po	^{214}Pb	3.1 min	112.1	16.4 ± 5.3	31.5
^{214}Po	^{210}Pb	164 μs	149.1	19.9 ± 6.4	37.5
^{210}Po	^{206}Pb	138 d	103.0	15.6 ± 5.1	30.0

Table 4.1 Recoil distances of isotopes of the ^{238}U chain

Mother isotope	Daughter isotope	Half-life	E_{recoil} [keV]	$< d >$ [nm]	d_{max} [nm]
^{228}Th	^{224}Ra	1.9 y	96.8	14.6 ± 4.6	28.0
^{224}Ra	^{220}Rn	3.66 d	103.4	15.3 ± 4.9	29.0
^{220}Rn	^{216}Po	55.6 s	116.4	16.7 ± 5.4	31.5
^{216}Po	^{212}Bi	145 ms	128.0	18.1 ± 5.9	34.0
^{212}Bi	^{208}Tl	60.6 min	117.2	17.1 ± 5.6	32.5
^{212}Po	^{208}Pb	299 ns	168.9	21.7 ± 7.1	41.4

Table 4.2 Recoil distances of isotopes of the ^{228}Th chain

Radon mitigation by applying a layer of coating can be successful only if the decay products of the contaminating radioactive mother isotope cannot be expected to traverse the entire width of the coating material. The layer thickness of the coating must therefore exceed the maximum possible total recoil distance that can be achieved by the relevant successive decays in the chain. Since ^{226}Ra has a half-life of 1.6 ky, decays occuring earlier in the ^{238}U chain are deemed to have an inconsequential effect on the total recoil range distribution within the coating. Similarly, only decays up to ^{214}Po are taken into account since its daughter ^{210}Pb has a half-life of 22.3 years. The number of decays occuring after this point is therefore assumed to be negligible considering the time scales on which we operate. Fig. 4.2 shows the probability distribution of the cumulative recoil ranges of successive isotopes of the ^{228}Th (blue) and ^{226}Ra (green) decay chains. The ranges d, at which 99% of all recoils are stopped, are indicated with dotted lines.

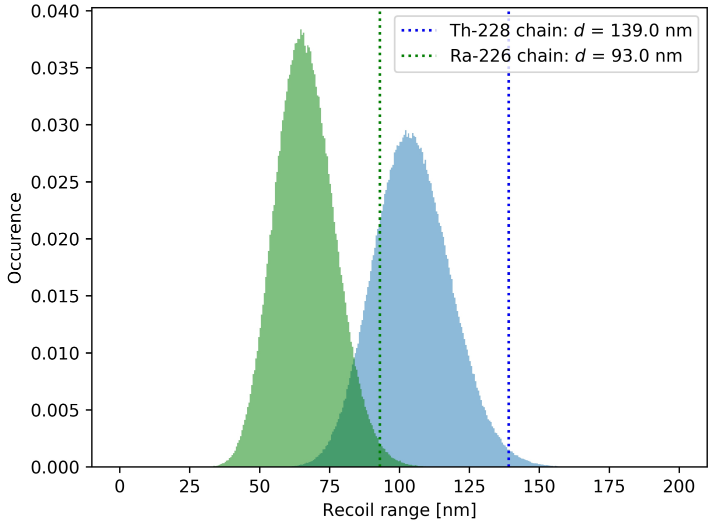

Fig. 4.2 Probability distributions of the total recoil range that can be achieved by isotopes of the ^{226}Ra (up to the decay of ^{214}Po) and ^{228}Th chains. The 99th percentiles are represented as dotted lines. Recoil range data simulated using SRIM.

Since 99% of the decay products of the ^{228}Th chain are expected to be blocked by a copper layer of d = 139 nm thickness, a coating of d = 5000 nm as was used in previous studies (see next section) should be sufficient to block all recoil-induced activity of the thoriated tungsten welding rods.

4.2 Previous results

Previous results conducted at the MPI for Nuclear Physics in Heidelberg (see [26] for details) suggest that it is possible to achieve reduction factors of at least up to 100 for ^{212}Pb, and 7.9 for ^{222}Rn by electrodeposition of copper. This result was obtained using seven thoriated tungsten welding rods of the same type as those used during the course of this work, coated individually in a 0.05 M/L $CuSO_4$ + 1 M/L H_2SO_4 electrolyte using a platinum counter electrode. The results of this study are summarized in table 4.3 below, where N is the number of rods coated, j indicates the average surface current density during coating, d is the targeted coating thickness, and R is the reduction factor.

Sample	N	j [mA/cm^2]	d [μm]	$R_{^{222}\text{Rn}}$	$R_{^{220}\text{Rn}}$
WTh_0a	1	5.3	10	–	107 ± 14
WTh_0b	1	5.5	5	–	47.4 ± 4.3
WTh_0c	7	5.9	5	7.9 ± 2.6	129 ± 3

Table 4.3 Reduction factors previously achieved with electrodeposited copper using a 0.05 M/L $CuSO_4$ + 1 M/L H_2SO_4 and a platinum counter electrode. Data taken from [26].

One of the goals for this thesis was to test whether these results are reproducible on larger scales. For this purpose, the multi-slot electrodeposition setup introduced in Ch. 3.3.1 was built. The results of this study are presented in the section below and compared to the previously achieved reduction factors listed in table 4.3.

4.3 Reduction factors achieved by electrodeposited copper

The multi-slot coating setup described in Ch. 3.3.1 was used to electrodeposit a layer of copper on the thoriated tungsten welding rods introduced in Ch. 3.1.2. In order to be able to compare findings from this work to previous results, the total coating layer thickness of 5 μm was kept. It was shown in section 4.1 that this should be sufficient to block all emanation caused by recoils from the ^{238}U and ^{228}Th chains.

Two batches (sample WTh_1 and WTh_2) of thoriated tungsten welding rods were coated to study the reduction factor achieved by copper coating produced following the procedure described in Ch. 3.3.1. As has been mentioned in Ch. 2.4, columnar copper growth can be an issue that facilitates the diffusion process of gaseous radon. Since the growth of electrodeposited copper is dependent on the surface current density [CITE], the second batch was coated by successively applying two different surface current densities in order to test whether the growth patterns could be broken. Succeeding in this could potentially reduce diffusion-driven radon emanation. Both sample batches were coated using a copper counter electrode and 5 L of 0.5 M/L $CuSO_4$ + 1 M/L H_2SO_4 electrolyte.

Sample WTh_1 consists of 31 thoriated welding rods from the batch ordered in 2017 (referred to as order 1 in table 4.4). The rods were divided into five batches of five and two batches of three rods each. All batches were coated from both sides by applying an average surface current density of $j = (69.6 \pm 0.6)$ mA/cm^2 until a coating thickness of 5 μm was achieved. The distribution of the mass increases is shown in fig. 3.8. The activities before and after coating were measured using the miniaturized proportional counters introduced in Ch. 3.2.3, allowing a determination of the ^{222}Rn reduction factor. Additionally, the emanation rate after coating was measured using a radon monitor.

Sample WTh_2 comprises 30 rods from the batch ordered in 2019 (order 2). The sample was measured before coating in both the miniaturized proportional counters and the radon monitor. Ten of these rods (**Sample WTh_2a**) were coated by applying an average initial surface current density of $j = (71.8 \pm 0.6)$ mA/cm^2 until a layer thickness of $d = 2$ μm was reached, then lowering the current density to $j = (6.4 \pm 0.1)$ mA/cm^2 for a further 3 μm. As mentioned above, this was done in order to test whether potential columnar growth patterns could be broken in an attempt to create a more diffusion-tight coating layer. These parameters were chosen such that the total path length of 5 μm from rod to coating surface would remain the same for samples WTh_1 and WTh_2. This means that any difference in reduction factor would be caused by a change in layer tightness rather than the thickness of the coating.
It is worth noting that a large number of copper sulphate crystals had precipitated in the electrolyte before coating sample WTh_2, indicating an oversaturation of $CuSO_4$. This was likely caused by continuous evaporation of sulphuric acid from the solution and re-filling of undiluted electrolyte over the course of around a month. This change in electrolyte concentration may have impacted the resulting coating structures, which should be kept in mind when considering the results. The activity of sample WTh_2a after coating was measured in a radon monitor.

Table 4.4 shows an overview of the sample size N, batch order (1 indicating the rods ordered in 2017, 2 the ones in 2019), and activities A of each sample. The ^{222}Rn activity was determined using miniaturized proportional counters. The ^{212}Po activity was measured using a radon monitor and serves as a proxy for the sample's ^{220}Rn emanation rate.

Even though the ^{212}Po activity of the uncoated rods of sample WTh_1 was not measured during the course of this study, earlier radon monitor measurements (see Ch. 4.2) taken of rods ordered at the same time allow an estimatation of the expected emanation rate. The previously measured ^{212}Po activity is consistent with that found for sample WTh_2 (see table 4.4), inspiring confidence that their ^{220}Rn emanation rate is comparable. Since the larger sample size of 30 rods leaves less room for error, the ^{212}Po activity found for the uncoated rods of sample WTh_2 was taken and extrapolated to 31 rods. This value was then used to find the corresponding reduction factor for sample WTh_1. As the original activity of sample WTh_2a was measured only as part of sample WTh_2, it was again assumed that the ^{212}Po activity is equal for all rods that were measured.

Sample	N	Order	$A_{^{222}\mathrm{Rn}}$[mBq]	$A^{\mathrm{coated}}_{^{222}\mathrm{Rn}}$ [mBq]	$A_{^{212}\mathrm{Po}}$ [mBq]	$A^{\mathrm{coated}}_{^{212}\mathrm{Po}}$ [mBq]
WTh_1	31	1	2.26 ± 0.10	1.29 ± 0.06	*395.5 ± 1.1*	29.4 ± 0.3
WTh_2	30	2	4.01 ± 0.17	–	382.7 ± 1.1	–
WTh_2a	10	2	–	–	*127.6 ± 0.4*	70.4 ± 0.6

Table 4.4 Activity before and after coating of samples 1 and 2. Values printed in italic are extrapolated from $A_{^{212}\mathrm{Po}}$ of sample WTh_2.

The reduction factors

$$R = \frac{A_{\mathrm{uncoated}}}{A_{\mathrm{coated}}} \tag{4.2}$$

achieved are summarized in table 4.5, along with the average surface current density j.

Sample	j [mA/cm^2]	$R_{^{222}\mathrm{Rn}}$	$R_{^{212}\mathrm{Po}}$
WTh_1	$\underset{5\mu\mathrm{m}}{69.6}$	**1.8 ± 0.1**	**13.5 ± 0.2**[1]
WTh_2a	$\underset{2\mu\mathrm{m}}{71.8} \rightarrow \underset{3\mu\mathrm{m}}{6.4}$	–	**1.8 ± 0.2**

Table 4.5 Reduction factors achieved using different surface current densities.

[1] Calculated under the assumption that the average ^{220}Rn content of the first batch equals that of the second.

The difference in the reduction factors of ^{222}Rn and ^{212}Po shown in table 4.5 was also seen in previous results (see table 4.3). A possible explanation is the difference of the half-lives of the gaseous radon isotopes ^{222}Rn and ^{220}Rn, where $T_{1/2,^{222}\mathrm{Rn}} = 3.8$ d and $T_{1/2,^{220}\mathrm{Rn}} = 56$ s. This means that the former has much longer to diffuse through the coating layer before it decays, thereby effectively increasing the amount of diffusion-driven emanation. It is expected that different surface current densities generate different types of structure of the electrodeposited copper. Additionally, the structure of the substrate on which the copper is deposited influences the growth of the new layer [5]. For the two-step coating process with the same initial surface current density that is then lowered by a factor of ten it is therefore expected that the coating becomes tighter at best due to a shift in the grain boundaries or continues grow as before at worst. In the first case, we would see an increased reduction factor, which would be an indicator that the grain structure is not bound to continue the growth pattern of the seed layer. In the second case, the growth pattern of the seed layer would continue regardless of the change in surface current density and the resulting reduction factor would remain comparable to the result seen for sample WTh_1. However, neither of these options is the case. Instead, we see that the reduction factor has decreased by a factor of 7.5. Since there are indications that the electrolyte concentration has changed between the coatings of sample WTh_1 and WTh_2a, however, it is not clear whether this is an effect caused by the change in surface current density or whether the amount of copper ions in the solution played a role.

The reduction factors seen in table 4.5 are all between 4 and 11 times lower than the previous results listed in table 4.3. Three parameters of the coating process were changed from the previous to the current coating process: the surface current density, the electrolyte concentration, and the material of the counter electrode. In order to investigate whether any of these parameters are directly responsible for the discrepancy, additional testing was conducted on non-thoriated welding rods. The results are presented in the next section.

4.4 Structural integrity of electrodeposited copper

The coatings produced within the scope of the previous study were all produced using a platinum counter electrode (see fig. 4.3) and an electrolyte concentration of 0.05 M/L $CuSO_4$ + 1 M/L H_2SO_4 electrolyte. Additionally, a much lower surface current density of around 6 mA/cm^2 table (see table 4.3) was applied to the rods compared to the average initial current density of 70 mA/cm^2 (see table 4.5) used for this work. The reason for this is that the initial surface current density is one of the factors on which the the adhesiveness of a coating layer is dependent [CITE]. It was found during pre-testing that below a certain threshold, the coating would wipe off easily even using just precision wipes, while at higher surface current densities it would pass the tape test described in Ch. 3.6. It is assumed that the interdependence between the electrolyte concentration, material of the counter electrode, and current play a role in determining the minimum suface current density necessary to create an adhesive layer. This could be a reason why it was possible to apply a much lower initial surface current density during previous studies and still achieve stable coating compared to the coatings created in this work.

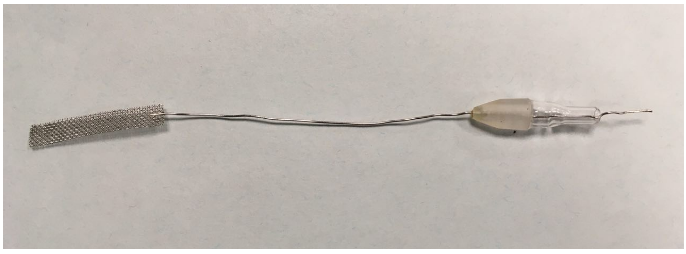

Fig. 4.3 Platinum counter electrode with a large surface area due to mesh structure.

The following tests were conducted on non-thoriated tungsten welding electrodes with a diameter of d = 4.8 mm and a length of l = 17.5 cm with the purpose of investigating the reason for the difference between former and current reduction factors. The samples were coated in a 300 mL beaker holding one sample at a time. Each sample was cleaned before being coated; some were wiped only with isopropanol (IPA), some additionally treated with acetone (ace) and de-ionized water (DIW). In case of the latter, the cleaning procedure is meant to replicate that used to obtain the previous results. The parameters that were varied are the surface current density j, the type of counter electrode CE, and the concentratration c of $CuSO_4$ in the electrolyte. A tape test using Pressure Sensitive Scotch™ tape (see Ch. 3.6) was conducted after each run to test the adhesiveness of the coating.

The results are listed in table 4.6 below.

Sample	Cleaning Procedure	CE	c [mol/L]	j [mA/cm^2]	Passed tape test
W_3a	IPA (1 ×)	Cu	0.05	$\underset{2\mu\mathrm{m}}{36} \rightarrow \underset{3\mu\mathrm{m}}{5}$	No
W_3b	IPA (1 ×)	Cu	0.05	$\underset{3.5\mu\mathrm{m}}{78}$	No
W_3c	IPA (1 ×)	Cu	0.05	$\underset{2\mu\mathrm{m}}{118} \rightarrow \underset{3\mu\mathrm{m}}{7}$	No
W_4a	IPA (1 ×)	Pt	0.05	$\underset{4.2\mu\mathrm{m}}{10}$	No
W_4b	ace (2 ×), IPA (2 ×), DIW (2×)	Pt	0.05	$\underset{4\mu\mathrm{m}}{7}$	No

Table 4.6 Coating specifications and tape test results of non-thoriated tungsten welding rods.

As presented in table 4.6, none of the coatings passed the tape test. It should be noted that generally, coatings produced using a higher initial surface current density seemed to be somewhat sturdier than those produced with low initial current density. As this is a qualitative observation only, no distinction was made between these subtle differences and all samples were classified as not having passed the test.
Sample WTh_4b was coated following the procedure used to coat sample WTh_0c of the previous study. According to [26], sample WTh_0c passed the tape test, unlike sample W_4b. Unfortunately however, the type of tape used in the previous study was not documented in [26]. It is therefore not certain whether sample WTh_0c passed the test due to superior adhesiveness of the coating or because of different test conditions. Since it is impossible to tell from the tape test alone whether their coating structures differ, two thoriated welding electrodes taken from sample WTh_2 were coated using the same parameters and their emanation rate measured in a radon monitor. The sample was pre-treated as described in [26]. For comparison, the original seven rods of sample WTh_0c were re-measured using the same monitor. The results are listed in table 4.7, along with the relevant coating parameters.

Sample	j [mA/cm^2]	CE	c[mol/L]	$A_{^{212}\mathrm{Po}}$ [mBq]	$A_{^{212}\mathrm{Po},\ \mathrm{coated}}$ [mBq]	$R_{^{212}\mathrm{Po}}$
WTh_5	$\underset{5\mu\mathrm{m}}{12.5}$	Pt	0.05	25.5 ± 0.1	17.3 ± 0.8	**1.5 ± 0.1**
WTh_0c	$\underset{5\mu\mathrm{m}}{7.9}$	Pt	0.05	91.12 ± 0.16	0.98 ± 0.15	**93.1 ± 14.3**

Table 4.7 Reduction factors of thoriated welding rods coated following the same procedure using a platinum counter electrode and 0.05-M $CuSO_4$ electrolyte. Activities measured using the same radon monitor.

As can be seen from table 4.7, the reduction factor of sample WTh_5 is a factor of 60 lower than that of sample WTh_0c despite having been coated under similar conditions and having undergone the same pre-coating cleaning procedure. Since the original rods were re-measured using the same radon monitor, issues with the detector can be ruled out as reason for this result. Further testing will need to be conducted in the future to determine what may have caused this discrepancy.

4.5 Temperature dependence of diffusion

As described in Ch. 2.2, we expect a diffusion-driven emanation process to exhibit a temperature dependence according to eq. 2.2. It was shown in Ch. 4.1 that the thickness of coating should be more than sufficient to stop any emenation caused by recoil, therefore we would expect the activity remaining after coating to be dominated by diffusion. The setup introduced in Ch. 3.4 was designed in order to investigate whether this is the case. For this purpose, ten thoriated tungsten welding rods from the batch ordered in 2019 were placed inside the emanation vessel, which was cooled down from room temperature to -90°C in several steps (referred to as first run in this section). Each temperature was maintained for around three days in order to give the emanation rate sufficient time to reach equilibrium. Gaseous radon reaching the emanation vessel was pumped into the detector volume of the radon monitor along with N_2, where the activity was measured according to the detection principle described in Ch. 3.2.1. The process was repeated in reverse order after the rods had been coated using the same parameters that were used to coat sample WTh_2a (referred to as second run). The bath temperature within the Dewar (T_{bath}) was kept uniform by using a stirrer. For the data points taken at room temperature, the Dewar was removed. The 50°C measurement was achieved by wrapping a heating blanket around the vessel.

In order to better understand any systematics of the setup that might have an impact on the result, the detector pressure and temperature inside the emanation vessel (T_{vessel}) were monitored throughout the experiment. The latter was achieved by attaching a Greisinger Pt100 sensor to the top flange of the emanation vessel such that the first ~ 5 cm of the probe were inside the vessel. The bath temperature was controlled using a Pt100 sensor connected to the HAAKE EK 90 immersion cooler. These parameters are analyzed in section 4.5.1. The result of the corresponding emanation measurements are investigated in section 4.5.2.

4.5.1 Systematic effects of the setup

Correlation between $\mathbf{T_{bath}}$ and $\mathbf{T_{vessel}}$

Fig. 4.4 shows the temperature settings of the immersion cooler (T_{bath}) plotted against the temeperature measured by the the Greisinger sensor (T_{vessel}). Data taken during the run for the uncoated rods is shown in black, the measurements for the coated rods are indicated in red.

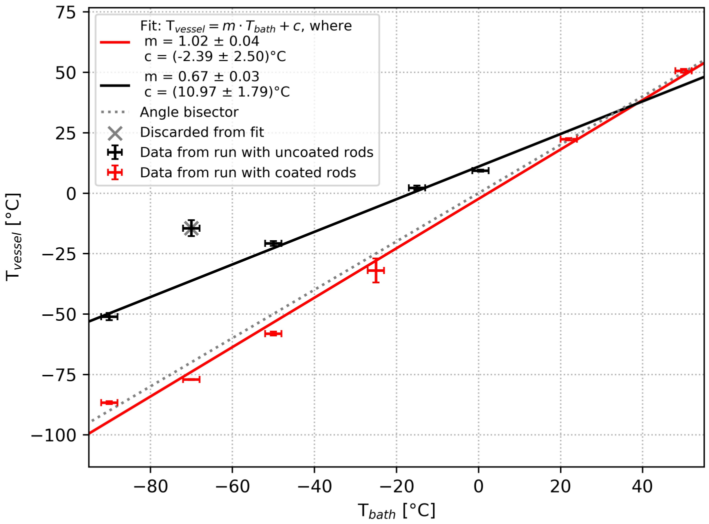

Fig. 4.4 Temperature measured inside the emanation vessel vs. bath temperature.

As can be seen in fig. 4.4, there is a close correlation between the bath temperature and the temperature measured using the Greisinger sensor during the measurement of the coated rods. Compared to this, the data taken for the uncoated rods seems to follow less of a linear relationship at a first glance. The discrepancy is most likely caused by the emanation vessel not being fully immersed in the cooling fluid, effectively creating a temperature gradient from top to bottom. The Greisinger sensor was located near the top of the flange where the effect was the strongest. This is reflected by the systematically higher temperature measured for the first run in fig. 4.4.

During the measurement of the uncoated rods, ambient moisture had formed a layer of ice around the top of the emanation vessel at temperatures below the freezing point of water. The outlier at -70°C coincides with a measurement during which a particularly thick layer of ice had formed over the weekend, which froze the stirrer in place. Without agitiation, the temperature gradient across the cooling fluid is expected to have increased. The ice was removed using a heat gun before the next measurement (at T_{bath} = -90°C) was started. The data point at T_{bath} = -70° was excluded for a more accurate fit. Without this outlier, a linear correlation between the set and measured temperatures can be found for the first run.

In order to prevent future ice formation, a protective layer of aluminium foil was placed around the top of the Dewar for the second run. Additionally, in order to obtain a more accurate reading of the temperature inside the emanation vessel, the Greisinger sensor was modified such that the tip was closer to the center of the vessel instead of near the top. The close match between T_{bath} and T_{vessel} for the second run shows that these steps were successful.

Temperature dependence of the pressure

According to the ideal gas law[2], the detector pressure should scale linearly with the temperature provided that the number of gas atoms within the volume remains constant. Fig.

---

[2] $PV = nRT$, where P is the pressure, V the volume, and T the absolute temperature of the gas, and n and R are the number of moles of gas and the ideal gas constant, respectively.

4.5 shows the bath temperature plotted against the average detector pressure.

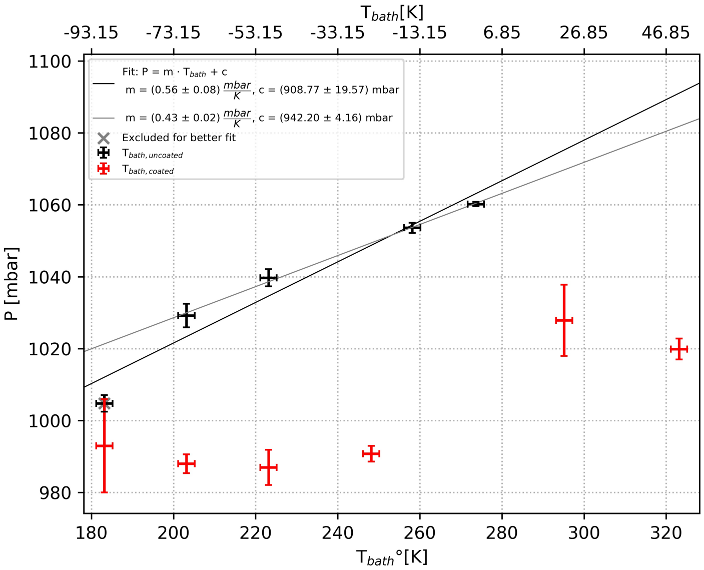

Fig. 4.5 Temperature dependence of the detector pressure

As can be seen in fig. 4.5, the linear model fits the data of the uncoated rods well if the point at -90°C is excluded. This data point was the first one taken after removing the ice and adding the aluminium foil. It is possible that this change in setup caused the point to deviate from the correlation found for the other data.

While the temperature dependence of the pressure shows the expected behaviour during the first run, this is certainly not the case during the second. Instead of the anticipated rise in pressure with the teperature, it remains at a relatively constant level of (990 ± 3) mbar for temperatures between -90°C and -25°C. This might be explained by a leak in the temperature sensor after it was modified. Since the connection piece between sensor and emanation vessel is not gas-tight by default, a rubber sealant had to be manually applied to the interface between the separate pieces. Additionally, it was found during dismounting of the emanation vessel that the screws connecting the top flange to the vessel had loosened. This was most likely caused by material contraction due to the drop in temperature. It is reasonable to assume that a combination of these two factors contributed to the creation of a sizeable leak.

Since the leak rate is dependent on the difference between the internal and external pressure [37], it is expected to be smaller for lower temperatures where the measured detector pressure is closer to that of the ambient air. If the temperature-induced increase in pressure exceeded the total leak rate integrated over the runtime, the average net pressure inside the detector would still increase. At the same time, we expect a gradual drop in pressure once the temperature has reached an equilibrium.

This behaviour is exactly what can be seen for the measurements at T_{bath} = 22°C and T_{bath} = 50°C. The measured pressure P and vessel temperature T_{vessel} are graphed in fig. 4.6.

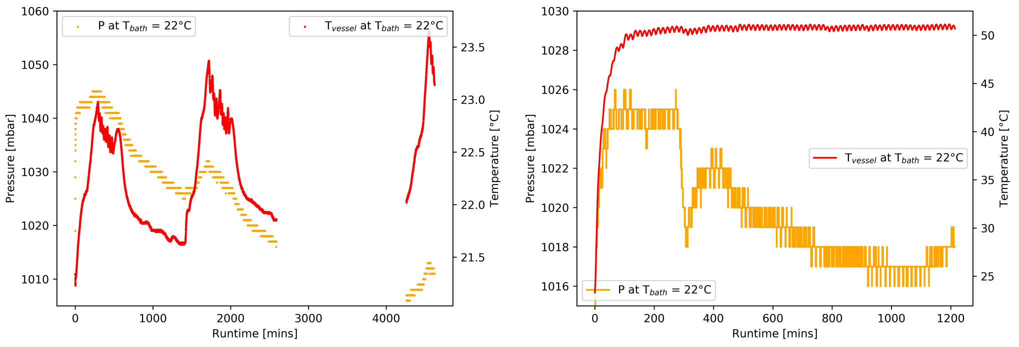

Fig. 4.6 Pressure and temperature development of the radon monitor for T$_{bath}$ = 22°C (*left*) and T$_{bath}$ = 50°C (*right*)

The temperature and pressure peaks seen in the left plot at 300, 1700, and 4550 minutes correspond to 24 hr cycles and are caused by changes in the ambient temperature during the day. A bug in the program caused a lapse in data-taking between 2500 and 4500 minutes runtime. For both measurements, any peaks and drops in the pressure coincide with those of the temperature. Overall, the pressure exhibits the aforementioned anticipated downwards trend, indicating that there was, indeed, a leak.

It was found that the detection efficiency of the radon monitor used varies up to 5% with its pressure [36]. Since the pressure was held nearly constant during the majority of the run due to the suspected leak, this effect was deemed negligible for the following considerations.

4.5.2 Temperature dependence of ^{212}Po activity

The Arrhenius equation (eq. 2.2) describes the expected dependency of the diffusion rate on the temperature. In order to verify whether the activity remaining after coating is driven by diffusion, ten thoriated tungsten welding rods coated with an average surface current density of $\underset{2\mu m}{72.8} \rightarrow \underset{3\mu m}{6.2}$ were placed inside the emanation vessel and their emanation rate measured. The detected ^{212}Po activities are plotted against the bath temperature T$_{bath}$ in fig. 4.7.

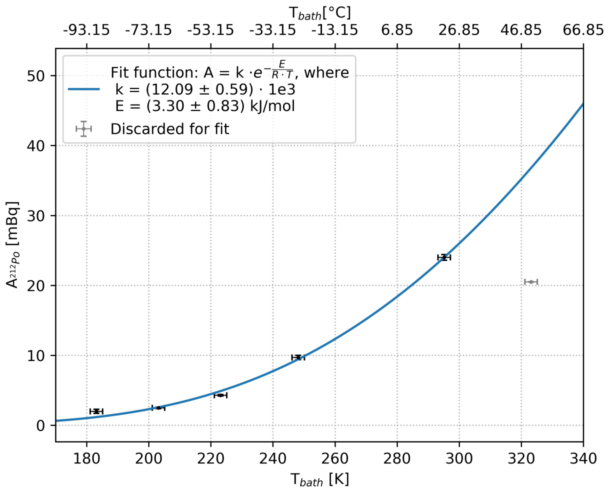

Fig. 4.7 ^{212}Po activity of the coated rods at varying bath temperatures

As can be seen from fig. 4.7, all but the data point at T_{bath} = 50°C show a ^{212}Po activity that is consistent with the model given by the Arrhenius equation. This indicates that the remaining activity is indeed driven by diffusion as the nuclear recoil process is not temperature dependent.

Meanwhile, the ^{212}Po activity at T_{bath} = 50°C is around a factor of 2.2 lower than predicted by the model. No specific tests were conducted to pinpoint the cause for this deviation. However, the emanation rate of the coated rods was measured in the same radon monitor that was used for samples WTh_1 and WTh_2 after the temperature dependence measurement was finished. This measurement showed a ^{212}Po activity of $A_{^{212}Po} = (10.0 \pm 0.2)$ mBq. Again using the original ^{212}Po activity of sample WTh_2 as the uncoated emanation rate, this yields a reduction factor of $R_{^{212}Po} = 12.8 \pm 0.3$.

This result is discussed in the next section, along with an interpretation of what might have caused it. The sample will be referred to as **Sample WTh_6**.

4.6 Conclusion and interpretation

Table 4.8 provides an overview of all releavant emanation measurements that were presented in this chapter.

Sample	N	c[mol/L]	CE	j [mA/cm^2]	Tape test	$R_{^{222}Rn}$	$R_{^{212}Po}$
WTh_0c[1]	7	0.05	Pt	$\underset{5\mu m}{5.9}$	Yes	7.9 ± 2.6	129 ± 3
WTh_1	31	0.5	Cu	$\underset{5\mu m}{70}$	Yes	**1.8 ± 0.1**	**13.5 ± 0.2**
WTh_2a	10	0.5	Cu	$\underset{2\mu m}{70} \rightarrow \underset{3\mu m}{7}$	Yes	–	**1.8 ± 0.2**
W_3a	5	0.05	Cu	$\underset{2\mu}{36} \rightarrow \underset{3\mu m}{5}$	No	–	–
W_3b	5	0.05	Cu	$\underset{2\mu}{78}$	No	–	–
W_3c	5	0.05	Cu	$\underset{2\mu}{118} \rightarrow \underset{3\mu m}{7}$	No	–	–
W_4a	1	0.05	Pt	$\underset{4.2\mu m}{10}$	No	–	–
W_4b	2	0.05	Pt	$\underset{4\mu m}{7}$	No	–	–
WTh_5	2	0.05	Pt	$\underset{5\mu m}{12.5}$	–	–	**1.5 ± 0.1**
WTh_0c[2]	2	0.05	Pt	$\underset{5\mu m}{12.5}$	Yes [3]	–	**93.1 ± 14.3**
WTh_6	10	0.5	Cu	$\underset{2\mu}{72.8} \rightarrow \underset{3\mu m}{6.2}$	–	–	**12.8 ± 0.3**

Table 4.8 Overview of all coating results

[1] Measured in 2017

[2] Measured in 2019

[3] Result by proxy; the tape test was conducted on a non-thoriated sample coated in the same way in 2017.

In section 4.3, we tested whether the previously achieved reduction factor of $R_{^{212}Po} \sim 130$ is reproducible using a different counter electrode, electrolyte concentration, and surface current density. It was found that the reduction factor using a copper counter electrode, 0.5 M/L $CuSO_4$ + 1 M/L H_2SO_4 electrolyte and a surface current density of ~ 70 mA/cm^2 (sample WTh_1) yields a reduction factor that is around ten times lower than the result found using a platinum counter electrode in a 0.05 M/L $CuSO_4$ electrolyte with a surface current density of ~ 6 mA/cm^2 (sample WTh_0c). It was shown in section 4.1 that a coating layer thickness of 5 μm should be more than sufficient to block all emanation originating from succesive decays of the ^{228}Th and ^{238}U chains in copper. Therefore it was suspected that the high emanation rate for sample WTh_1 was caused by a columnar copper growth, effectively creating diffusion highways through which gaseous radon could diffuse out of the coating substrate. As growth patterns during electrodeposition are highly dependent on surrounding conditions such as potential [5, 25] , an attempt was made to break the growth pattern by applying a lower current density of around 7 mA/cm^2 after the initial 2 μm of coating. This was expected to either increase the reduction factor if successful, or yield the same reduction if changing the current density had no effect on growth process. Surprisingly, the reduction factor instead dropped to $R_{^{212}Po} = 1.8$. As the initial surface current density was not affected by this change, the first 2 μm should have been deposited in the same way as for sample WTh_1. The stark deviation of the reduction factor from that obtained for sample WTh_1 is an indication that some change had occured in a coating parameter that had not been considered previously. As it was noticed before coating sample WTh_2a that an unusually large amount of copper crystals from the electrolyte had precipitated, we suspect that an oversaturation of the electrolyte caused a change in the deposition behaviour. However, this process is not yet fully understood and requires further investigation. Since base layer coated with the initial surface current density matching that used for sample WTh_1 is likely to have been influenced by the change in electrolyte concentration as well, this result yield no information about the potential effect of changing the surface current density during the coating process.

However, there is one related result that was obtained within the context of measurement of the temperature dependence of diffusion-driven emanation. As can be seen in the overview table 4.8, sample WTh_6 was coated using nearly identical parameters as were used for the coating of sample WTh_2a. The coating process took place one week before the coating of sample WTh_2a and the amount of precipitation in the electrolyte, although present, was notably smaller. While it should be noted that the emanation measurement of the coated rods at room temperature took place after the samples had already been cooled down to -90°C, the result might still be of interest.
The ^{212}Po activity of the coated rods at $T_{bath} = 22$°C was $A_{^{212}Po} = (24.0 \pm 0.4)$ mBq, while a measurement of the uncoated rods in the same setup at room temperature yielded an activity of $A_{^{212}Po} = (120.1 \pm 2.1)$ mBq. This leads to a reduction factor of $R_{^{212}Po} = 5.0 \pm 0.1$, which is a factor of ~ 2.5 higher than the reduction factor found for sample WTh_2a. It is also still lower than the reduction factor achieved for sample WTh_1. Since the electrolyte was not freshly made and some amount of precipitation was seen it is not clear to what extent a possible change in copper ion concentration has impacted the coating process of sample WTh_6. Nonetheless, this is an indication that the concentration of copper ions in the solution might indeed have an impact on the resulting structure of the electrodeposited copper.

The temperature dependence measurement yielded another interesting result: as was mentioned in section 4.5.2, all measurements but that at $T_{bath} = 50$°C are consistent with the temperature dependence model given by the Arrhenius eq. 2.2. For $T_{bath} = 50$°C, the ^{212}Po activity is a factor of around 2 lower than expected. The temperature, pressure, and gas flow data (see fig. 4.6 for the first two parameters) for this particular measurement is, however, inconspicuous, and no external disturbances could be found that might explain this result. In the absence of obvious anomalies, we can make an educated guess about the origin of this deviation. Recrystallization is a process by which deformed grains are replaced by a new set of strain-free and equiaxed grains that begin as small nuclei and grow until they have replaced the parent material entirely [39]. Such processes are known to occur over a period of time from years down to several hours, even at temperatures as low as room temperature [40]. This process is accelerated by the heating of the substrate. It is possible that somewhere between the measurements at T_{bath} = 22°C and T_{bath} = 50°C, the coating material underwent an (accelerated) nucleation process. The resulting change in grain structure might have contributed to the change in the measured ^{212}Po activity. As was mentioned in section 4.5.2, this activity was re-measured in the radon monitor after the temperature dependence measurement. This yielded a ^{212}Po activity of A^{212}Po = (10.0 ± 0.2) mBq. As the detector recirculation setup likely has a different detection efficiency than the radon monitor used for this separate measurement, the activity of the coated rods is compared to the activity of sample WTh_2a (uncoated). The resulting reduction factor $R_{^{212}\mathrm{Po}} = 12.8 \pm 0.3$ is higher than the reduction factor estimated at T_{bath} = 22°C. This further supports the theory that it was not a detection error that caused the lower activity but rather a change inherent to the sample. This is, of course, merely speculation and further testing will be required. If this proves to be the case, it would be a promising approach to further improve the mitigation properties of electrodeposited copper since it explicitely targets diffusion-driven emanation.

This theory might also be able to explain another observation seen during the re-measurement of sample WTh_0c that was coated during previous studies (see section 4.4). It was found that the ^{212}Po reduction factor was $R_{^{212}\mathrm{Po}} = (93.1 \pm 14.3)$ for the re-measurement, compared to $R_{^{212}\mathrm{Po}} = (129 \pm 3)$ for the original conducted two years ago. The measurements were made using the same radon monitor and PIN diode. While the sample was not heated beyond normal temperature fluctuations during the day, this reduced reduction factor might also be caused by slower recrystallization processes taking place over the course of several years. If this is the case, more studies should be conducted in order to avoid losing reduction efficiency over time.

When trying to reproduce the previous results by applying the same coating procedure, a reduction factor of $R_{^{212}\mathrm{Po}} = (1.5 \pm 0.1)$ was achieved instead (see table 4.7). Here, it is entirely unclear what caused this significant difference. Sample WTh_5 was coated using fresh electrolyte and a Pt electrode of the same type as was used for sample WTh_0c. Further testing is required here as well to find the origin of this discrepancy.

It was shown in section 4.5.2 that since the ^{212}Po activity after coating exhibits a strong dependency on the temperature. This is consistent with the temperature dependency of the diffusion constant given by the Arrhenius equation eq. 2.2. This indicates that the majority of the residual activity after coating likely stems from diffusion processes. Given that the DARWIN cryostat is expected to operate at LXe temperatures around -90°C [38] where diffusion all but subsides, this is beneficial to the background reduction.

Summary and outlook

In this thesis, the suitability of electrodepostited copper coatings were studied for their potential use to lower the background in the prospective DARWIN dark matter search. DARWIN is an experiment set to employ liquid xenon to search for Weakly Interacting Massive Particles (WIMPs) and shares many characteristics with the XENON dark matter search, which it will replace. ^{222}Rn is the dominant source threatening the ultra-low background level required to reach the planned detection sensitivity of the DARWIN detector. Mitigating the emanation of this radioisotope, which permanently emanates from the detector materials, is therefore a key aspect on which the success of experiment depends. Recoil and diffusion are the two emanation mechanisms that can cause gaseous radon to reach the sensitive volume of the detector.

Within the context of this study, the suitability of an electrodeposited layer of coating is primarily characterized by the reduction factor it yields for the isotopes threatening the background level of the DARWIN detector. The emanation process of gaseous radon is caused by both diffusion and recoil. This requires a viable coating layer to both be thick enough to stop recoil and tight enough to stop diffusion. Furthermore, it is important that its structural properties remain stable under operational conditions. These characteristics were studied using thoriated tungsten electrodes as a radon source. The welding rods emanate both ^{220}Rn and ^{222}Rn. Non-thoriated tungsten welding electrodes were used to study the mechanical properties of the coating layers by employing the tape test.

The ^{220}Rn activity of the welding electrodes before and after coating was measured using a radon monitor, their ^{222}Rn activity using miniaturized proportional counters that were originally developed for the GALLEX experiment.
Previous studies have hinted that 5μm of electrodeposited copper can achieve a reduction factor of up to ~ 129 for ^{220}Rn. This result could not be reproduced during the course of this work; the highest achieved reduction factor for ^{220}Rn was 13.5. Several parameters could be responsible for this deviation. The previous result was achieved by coating seven thoriated welding rods using a platinum counter electrode, an electrolyte concentration of 0.05 M/L $CuSO_4$ + 1 M/L H_2SO_4, and a surface current density of ~ 6 mA/cm^2. The reduction of 13.5 was found after coating 31 thoriated welding rods using a copper counter electrode, a 0.5 M/L $CuSO_4$ + 1 M/L H_2SO_4 electrolyte, and a surface current density of 70 mA/cm^2. It is not clear what exactly caused the difference, further tests are required to gain a clearer picture. A second result obtained by lowering the surface current density to 7 mA/cm^2 after approx. 2 μm of coating yielded an even lower ^{220}Rn reduction factor of 1.8. It is possible that this was caused by an oversaturation of the electrolyte, however this, too, remains to be studied more closely.
An attempt was made to recreate the previously achieved coating by using the same elec-

trolyte concentration, type of counter electrode, and surface current density. The resulting reduction factor of ~ 1.5 compared to the previously achieved factor of 129 shows that there must be parameters affecting the structure of the coating that have not yet been taken into account.
A measurement of the ^{212}Po activity of coated thoriated tungsten rods at different temperatures ranging from -90°C to 50°C is consistent with the temperature dependence of the diffusion constant given by the Arrhenius equation. This indicates that the majority of the remaining activity seen after the coating process is diffusion-driven.
This measurement had one deviant result: at a bath temperature of 50°C, the activity measured was a factor of approx. 2.2 lower than expected from the model given by the Arrhenius equation. A re-measurement using a different monitor showed that this was not a detection error. It is possible that the coating underwent an accelerated nucleation process between bath temperatures of 22°C and 50°C which effectively served to increase the reduction factor. Whether this is indeed the case remains to be studied, however if this proves to be true it could be a promising next step in the search for an electrodeposition process that can feasibly serve the reduction of the radon background in the search for dark matter.

Overall we can conclude that the electrodeposition process is not understood very well at this stage and that there are likely as yet unknown parameters that impact the structure of deposited coating.

Future of coating

Based on the results presented in this thesis it is clear that the subtelties of electrodeposition are not yet clearly understood and that achieving consistent coating results with electrodeposited copper is not trivial. In order to gain a better understanding about this topic, a collaboration between the MPIK and Prof. Stéphane Lucas of the university of Namur is currently in the works. It has been proposed to explore the possibility of using multiple layers of different coating materials in order to increase layer tightness such that a higher reduction of diffusion-driven emanation can be achieved. Additionally, the performance of polymer-based coatings will be explored.

Appendix A

SEM images

In order to better understand the effect using different coating parameters has on the resulting deposited coating, a number of SEM images were taken of coated, non-thoriated welding rods. The rods were cut to pieces of around one cm length using a small circular saw.

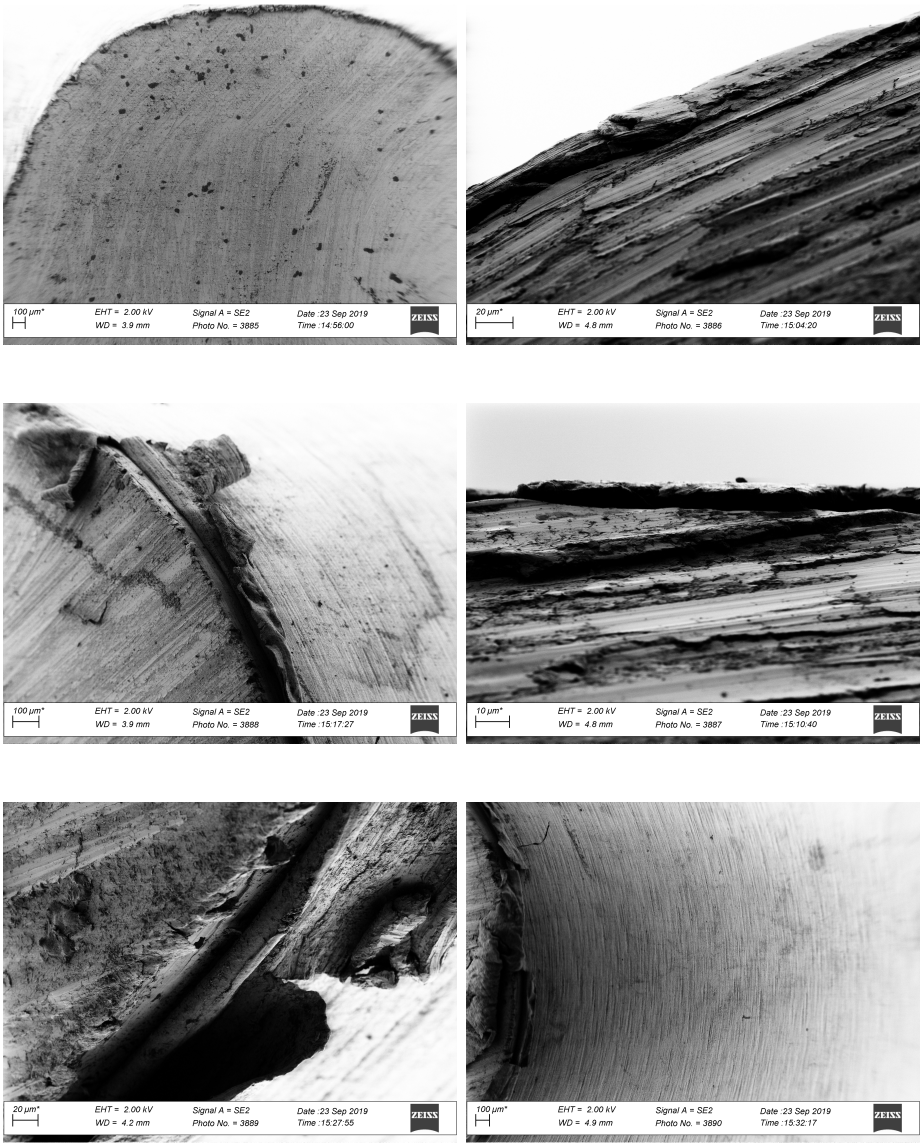

Fig. A.1 SEM images of coating deposited on non-thoriated tungsten welding rods. Images made with help of Sebastian Wurzbacher of the EMCF team.

List of Figures

List of Tables

Bibliography

[1] F. Zwicky, ”Die Rotverschiebung von extragalaktischen Nebeln”, *Helvetica Physica Acta* **6** (1966)

[2] [Planck Collaboration], ”Planck 2013 results. I. Overview of products and scientific results”,*Astonomy &Astrophysics* **573** (2014)

[3] G. Bertone et al., “Particle dark matter: Evidence, candidates and constraints,” *Physics Reports*, vol. **405**, no. 5, pp. 279–390 (2005)

[4] P. E. Rosenfeld, L. G. H. Feng, ”Risks of Hazardous Wastes”, William Andrew Publishing (2011)

[5] John Wiley & Sons, Inc., ”Modern Electroplating, Fifth Edition” (2010)

[6] G. Bertone, Dan Hooper, ”A History of Dark Matter”, *Rev. Mod. Phys.* **90**, 45002 (2018)

[7] Bessel, F.W. (1844), MNRAS **6**, 136

[8] E. Aprile *et al.* [XENON Collaboration], ”The XENON100 Dark Matter Experiment”, *Astroparticle Physics* **35** no. 9, pp. 573-590 (2012)

[9] K. Ni, ”The XENONnT Dark Matter Experiment”, Presentation for the DPF conference at Fermilab (2017)

[10] E. Aprile *et al.* [XENON Collaboration], ”Dark Matter Search Results from a One Ton-Year Exposure of XENON1T”, *Phys. Rev. Lett.* **121**, no. 11

[11] The XENON collaboration, ”Physics and reach of the XENON1T dark matter experiment”, *Journal of Cosmology and Astroparticle Physics* **2016** (April 2016)

[12] E. Aprile *et al.* [XENON Collaboration], ”DARWIN: Towards the ultimate dark matter detector *Journal of Cosmology and Astroparticle Physics* **2016** (Nov 2016)

[13] S. Bruenner, ”Mitigation of Rn-222 induced background in the XENON1T dark matter experiment”, University of Heidelberg (PhD thesis, 2017)

[14] E. Aprile *et al.* [XENON Collaboration], ”XENON1T Dark Matter Data Analysis: Signal & Background Models, and Statistical Interference”, *Phys.Rev. D99* no. **11** (2019)

[15] Internal wiki

[16] H. Mehrer, “Diffusion in solids: fundamentals, methods, materials, diffusion-controlled processes”, Springer (2007)

[17] W. Demtröder, "Experimentalphysik 4", Springer (2009)

[18] Paper in preparation

[19] P. Van Duppen and K. Riisager, "Physics with rex-isolde: from experiment to facility," *Journal of Physics G: Nuclear and Particle Physics* **38** no. 2, (2011)

[20] A. Kjelberg, G. Rudstam, "ISOLDE isotope separator on-line project", *CERN Courier* **7** (2): 22–27 (1967)

[21] A. Papageorgiou Koufidou, "Higher energies for ISOLDE's radioactive ion beams", *Accelerating News* **18** (2016)

[22] N. Norziehana Che Isa, Y. Mohd, M. H. M. Zaki, S. A. S. Mohamad, "Characterization of Copper Coating Electrodeposited on Stainless Steel Substrate",*Int. J. Electrochem. Sci.* **12** (2017)6010–6021

[23] N.D. Nikolic, L.J. Pavlovic, M.G. Pavlovic, K.I. Popov, "Effect of temperature on the electrodeposition of disperse copper deposits", *J. Serb. Chem. Soc.* **72** (12) (2007) 1369–1381

[24] S. Masciocchi, "Semiconductor detectors", talk for the 39th Heidelberg Physics Graduate Days (2017)

[25] J. W. Dini, "Electrodeposition – The Materials Science of Coatings and Substrates", *Advanced Materials* **6** 1, pp. 88-89 (1994)

[26] F. Joerg, "Investigation of coating-based radon barriers and studies towards their applicability in liquid xenon", Master's thesis at the University of Heidelberg (2017)

[27] P. Pagelkopf and J. Porstendörfer, "Neutralisation rate and the fraction of the positive 218po-clusters in air," *Atmospheric Environment*, vol. **37**, no. 8, pp. 1057 – 1064 (2003)

[28] P. Herrero Gómez, "Investigation of surface cleaning procedures for the removal of radon daughters from PTFE surfaces and their applicability in liquid xenon detectors", Master's thesis at the University of Heidelberg (2018)

[29] T. Skwarnicki, "A study of the radiative CASCADE transitions between the Upsilon-Prime and Upsilon resonances", Cracow, INP (1986)

[30] L. Fischer, "Investigation of Material Coatings in order to Reduce the Emanation of Radon", Bachelor's thesis at the University of Heidelberg (2016)

[31] R. Wink, P. Anselmann, D. Dörflinger, W. Hampel, G. Heusser, T. Kirsten, P. Mögel, E. Pernicka, R. Plaga and C. Schlosser, "The miniaturized proportional counter HD-2(Fe)/(Si) for the GALLEX solar neutrino experiment", *Nucl. Instrum. Methods Phys. Res. A* **329**(3), pp. 541-550 (1993)

[32] U. Schwarz, lecture notes for the course Statistical Physics (2017/2018)

[33] M. Drdácky *et al.*, "Standardization of peeling tests for assessing the cohesionand consolidation characteristics of historic stone surfaces", *Materials and Structures* **45** 505-520 (2012)

[34] J. Ziegler, J. Biersack, M. Ziegler, "SRIM: The Stopping and Range of Ions in Matter" (2008)

[35] M. T. Robinson, (1994) "The binary collision approximation: Background and introduction, Radiation Effects and Defects in Solids", *Radiation Effects and Defects in Solids* vol. null no.1, 3-20

[36] Internal communications

[37] Wutz, Adam, Walcher, Jousten, Vieweg, "Handbuch der Vakuumtechnik" (2000)

[38] E. Aprile *et al.* [XENON Collaboration], "The XENON1T Dark Matter Experiment", *The European Physical Journal* (2017)
`https://arxiv.org/pdf/1708.07051.pdf`

[39] G. Gottstein, "Physikalische Grundlagen der Materialkunde", Springer (2007)

[40] V.A. Vas'ko, I. Tabakovic, S.C. Riemer, "Structure and Room-Temperature Recrystallization of Electrodeposited Copper", *Electrochemical and Solid-State Letters*, **6** (7) C100-C102 (2003)

[41] R. Monroe, "Dark Matter", `xkcd` (2019)

Erklärung

Ich versichere, dass ich diese Arbeit selbstständig verfasst und keine anderen als die angegebenen Quellen und Hilfsmittel benutzt habe.

Heidelberg, den ....